Posted on 13 May 2023 — The copyright holder is the author/funder. All rights reserved. No reuse without permission. — https://doi.org/10.22541/essoar.168394754.48914569/v1 — This a preprint and has not been peer reviewed. Data may be preliminary.

A case study of the solar and lunar semidiurnal tide response to the 2013 sudden stratospheric warming

Willem Elias van Caspel[1], Patrick Joseph Espy[2], Robert E. Hibbins[2], Gunter Stober[3], Peter G. Brown[4], Christoph Jacobi[5], and Johan Kero[6]

[1]Meteorologisk institutt
[2]Norwegian University of Science and Technology
[3]University of Bern
[4]University of Western Ontario
[5]Institut fur Meteorologie, Universitat Leipzig, Germany
[6]Swedish Institute of Space Physics

May 13, 2023

Abstract

This study investigates the response of the semidiurnal tide (SDT) to the 2013 major sudden stratospheric warming (SSW) event using meteor radar wind observations and mechanistic tidal model simulations. In the model, the background atmosphere is constrained to meteorological fields from the Navy Global Environmental Model - High Altitude analysis system. The solar (thermal) and lunar (gravitational) SDT components are forced by incorporating hourly global temperature tendency fields from the ERA5 forecast model, and by specifying the M2 and N2 lunar gravitational potentials, respectively. The simulated SDT response is compared against meteor wind observations from the CMOR (43.3*N, 80.8*W), Collm (51.3*N, 13.0*E), and Kiruna (67.5*N, 20.1*E) radars, showing close agreement with the observed amplitude and phase variability. Numerical experiments investigate the individual roles of the solar and lunar SDT components in shaping the net SDT response. Further experiments isolate the impact of changing propagation conditions through the zonal mean background atmosphere, non-linear wave-wave interactions, and the SSW-induced stratospheric ozone redistribution. Results indicate that between 80-97 km altitude in the northern hemisphere mid-to-high latitudes the net SDT response is driven by the solar SDT component, which itself is shaped by changing propagation conditions through the zonal mean background atmosphere and by non-linear wave-wave interactions. In addition, it is demonstrated that as a result of the rapidly varying solar SDT during the SSW the contribution of the lunar SDT to the total measured tidal field can be significantly overestimated.

A case study of the solar and lunar semidiurnal tide response to the 2013 sudden stratospheric warming

Willem E. van Caspel[1,2,*], Patrick Espy[1,2], Robert Hibbins[1,2], Gunter Stober[3], Peter Brown[4], Christoph Jacobi[5], Johan Kero[6]

[1]Department of Physics, Norwegian University of Science and Technology (NTNU), Trondheim, Norway
[2]Birkeland Centre for Space Science, Bergen, Norway
[3]Institute of Applied Physics and Oeschger Center for Climate Change Research, Microwave Physics, University of Bern, Bern, Switzerland
[4]Department of Physics and Astronomy, Western University, London, Ontario, Canada
[5]Leipzig University, Leipzig, Germany
[6]Swedish Institute of Space Physics, Kiruna, Sweden

Key Points:

- Simulations of the SDT are compared against meteor wind observations in the mid-to-high latitude northern hemisphere during the 2013 SSW
- Individual lunar and solar SDT simulations find that the net tidal response is largely driven by the solar component
- The response of the solar SDT is driven by changing zonal mean propagation conditions and by non-linear interactions with planetary waves

* Now at Research and Development Department, Norwegian Meteorological Institute, Oslo, Norway

Corresponding author: Willem van Caspel, willemvc@met.no

Abstract

This study investigates the response of the semidiurnal tide (SDT) to the 2013 major sudden stratospheric warming (SSW) event using meteor radar wind observations and mechanistic tidal model simulations. In the model, the background atmosphere is constrained to meteorological fields from the Navy Global Environmental Model - High Altitude analysis system. The solar (thermal) and lunar (gravitational) SDT components are forced by incorporating hourly temperature tendency fields from the ERA5 forecast model, and by specifying the M_2 and N_2 lunar gravitational potentials, respectively. The simulated SDT response is compared against meteor wind observations from the CMOR (43.3°N, 80.8°W), Collm (51.3°N, 13.0°E), and Kiruna (67.5°N, 20.1°E) radars, showing close agreement with the observed amplitude and phase variability. Numerical experiments investigate the individual roles of the solar and lunar SDT components in shaping the net SDT response. Further experiments isolate the impact of changing propagation conditions through the zonal mean background atmosphere, non-linear wave-wave interactions, and the SSW-induced stratospheric ozone redistribution. Results indicate that between 80-97 km altitude in the northern hemisphere mid-to-high latitudes the net SDT response is driven by the solar SDT component, which itself is shaped by changing propagation conditions through the zonal mean background atmosphere and by non-linear wave-wave interactions. In addition, it is demonstrated that as a result of the rapidly varying solar SDT during the SSW the contribution of the lunar SDT to the total measured tidal field can be significantly overestimated.

1 Introduction

During wintertime, planetary waves can propagate upwards from the troposphere into the stratosphere (Charney & Drazin, 1961). There they can destabilize the westerly winds of the stratospheric polar vortex, potentially leading to a vortex split or displacement event. The planetary wave breaking associated with such events induces enhanced stratospheric poleward meridional flows, leading to rapid compressional heating, or sudden stratospheric warming (SSW). Moreover, the westward momentum forcing exerted by the planetary waves causes a reversal of the otherwise westerly winds. While most of the dynamical changes associated with SSWs occur in the mid- and high-latitude stratosphere, their impact can extend from the troposphere up into the thermosphere (Limpasuvan et al., 2016). In the mid- and high-latitude mesosphere-lower-thermosphere (MLT, 80-110 km altitude), one of the major sources of SSW variability is associated with the induced changes to the semidiurnal tide (SDT) (Baldwin et al., 2021).

The SDT is an atmospheric inertio-gravity wave that is expressed as a near 12-hour oscillation in the atmospheric winds, temperature and pressure fields (Chapman & Lindzen, 1970). While it is predominantly excited by radiative and latent heating in the lower atmosphere following the daily insulation cycle, the SDT reaches its largest amplitudes in the MLT due to the decreasing density of the atmosphere with altitude (Hagan, 1996). An additional excitation mechanism for the SDT arises from the lunar gravitational potential, which excites waves with near integer fractions of a lunar day periods. Through neutral atmosphere and ionosphere coupling, the different SDT components are also observed in ionospheric parameters such as equatorial E $\times$ B plasma drift velocities, F-region electron densities, ion temperatures, and sporadic E occurrence frequencies (Pedatella et al., 2014; Arras et al., 2009).

The SDT signature in the upper atmosphere is strongly influenced by the tidal propagation conditions through the underlying atmosphere (van Caspel et al., 2022). The SDT therefore represents an important coupling mechanism between the variability of the lower and middle atmosphere and that of the MLT and ionosphere system (Pedatella & Forbes, 2010; Forbes, 2009). This coupling is especially pronounced during SSWs, when tidal propagation conditions rapidly change (L. P. Goncharenko et al., 2021). However, open questions remain about the spatio-temporal drivers of the SDT response, in particular regarding the individual roles and driving mechanisms of the solar and lunar SDT components (L. P. Goncharenko et al., 2022; J. Liu et al., 2021; G. Liu et al., 2021; J. Zhang et al., 2021; Wu et al., 2019).

The SDT response is challenging to investigate due to the large number of physical mechanisms involved. These include changes to the propagation conditions of the individual solar (12.00 hr) and lunar M_2 (12.42 hr) and N_2 (12.64 hr) components (Forbes & Zhang, 2012; Jin et al., 2012), non-linear wave-wave interactions with quasi-stationary planetary waves (H.-L. Liu et al., 2010), and changes to the thermal forcing caused by a redistribution of stratospheric ozone (L. P. Goncharenko et al., 2012). Quantifying the individual contributions of these mechanisms to the net SDT response is further complicated by the need for time windows upwards of 15 days to separate the lunar and solar components from a single time series (J. Liu et al., 2021; Lin et al., 2019; X. Zhang & Forbes, 2014a). Such long time windows can easily lead to an overly smoothed and potentially cross-contaminated view of the SDT response, especially considering that SSW-induced SDT variability can occur over the course of a few days (Stober et al., 2020).

In this study, SDT observations from a range of Northern Hemisphere mid- and high-latitude meteor wind radars are simulated using a mechanistic tidal model during the 2013 major SSW event. The model, called the PRimitive equations In Spherical harmonics Model (PRISM), is a high-top neutral atmosphere model that allows for a free specification of the background atmosphere and tidal forcing terms (van Caspel et al., 2022). The background atmosphere is specified to realistic three-dimensional winds and temperatures, and the SDT is forced by incorporating a detailed thermal and gravitational forcing scheme. The gravitational scheme includes both the M_2 and N_2 lunar SDT components, and incorporates ocean and load tide elevation fields from a global ocean tidal model.

Section 2 describes the implementation of the solar and lunar tidal forcing terms, and of the background atmospheric specification. In Section 3, the simulated SDT response is compared to measurements from the CMOR (43.3°N, 80.8°W), Collm (51.3°N, 13.0°E), and Kiruna (67.5°N, 20.1°E) meteor wind radars between 80-97 km altitude. In addition, individual simulations of the lunar and solar SDT components are performed to establish the relative importance of these tidal components in shaping the net simulated SDT response. In Section 4, numerical experiments are performed to assess the impact of the changing propagation conditions through the zonal mean background atmosphere, non-linear wave-wave interactions with quasi-stationary planetary waves, and of changes to the thermal forcing resulting from a redistribution of stratospheric ozone. The results are discussed and concluded in Section 5.

2 Model Description

PRISM is a non-linear and time-dependent spectral model, which in earlier work has been used to simulate the SDT in the mid-latitude MLT (van Caspel et al., 2022). The model includes a climatological description of tidal dissipation terms through ion drag, Newtonian cooling, eddy diffusion, molecular diffusion, and surface friction. In this study, the horizontal resolution is truncated at zonal wavenumber S = 9 and meridional wavenumber N = 24, with 161 vertical levels up to an altitude of ∼430 km. While a detailed description of the model can be found in van Caspel et al. (2022) and references therein, those aspects of the model which have been modified for the current work are discussed below.

2.1 Background Atmosphere

The three-dimensional background atmosphere can be freely specified by relaxing the model's dynamical fields towards that of the input meteorology, for which a nudging rate of $D = 1/3$ days^{-1} (d^{-1}) is used. This nudging rate is high enough to accurately represent the spatial and temporal evolution of the polar vortex, while being low enough to have no effect on the simulated SDT wave-field. To minimize the effect of wave-mean flow interactions between the zonal mean background atmosphere and the artificially introduced planetary waves (Pedatella & Liu, 2013), the zonal mean spherical harmonic coefficients are nudged at a rate of $D_0 = 4\ \mathrm{d}^{-1}$. While this may damp non-migrating zonal mean SDT components, diagnostic simulations with a lower zonal mean nudging rate find that this tidal component does not contribute significantly to our results.

The background atmosphere between 85-0.001 hPa (approximately 10-95 km altitude) is nudged to daily mean wind and temperature fields calculated from 3-hourly NAVGEM-HA meteorological analysis data. The NAVGEM-HA model incorporates satellite observations of ozone, water vapor, and temperatures in the stratosphere and mesosphere, as well as standard operational meteorological observations in the troposphere (McCormack et al., 2017). Previous studies have shown that the NAVGEM-HA mean winds and temperatures are in good agreement with observations during the 2013 SSW event (Stober et al., 2020; McCormack et al., 2017).

Fig. 1a illustrates the temporal evolution of the 2013 SSW in both the daily mean NAVGEM-HA fields and in PRISM, using the definition of Polar Vortex Weakening (PVW) proposed by X. Zhang and Forbes (2014b). According to this definition, the day of peak PVW occurs on January 10th 2013. On this day, zonal mean zonal winds at 48 km altitude and 70°N reach their most easterly phase, coincident with zonal mean temperatures at 40 km altitude and 90°N reaching a maximum. Within the context of this work, the SSW onset is taken as the point where the zonal mean zonal winds at 48 km altitude and 70°N reverse, on January 3rd. The onset of the recovery phase is taken as the point where the zonal mean zonal winds return to their climatological westerlies, on January 22nd. However, throughout the following text, the onset date, day of peak PVW, and recovery phase are referred to by their number of days since the 1st of December 2012 (day 34, 41, and 53, respectively), which is the starting date of the simulations.

To demonstrate the accurate representation of the polar vortex in PRISM, Fig. 1b shows the evolution of quasi-stationary planetary waves with zonal wavenumber 1 (PW1) and 2 (PW2) in the NAVGEM-HA and PRISM zonal winds at 48 km altitude. The wave amplitudes are calculated by least-squares fitting stationary PW1 and PW2 waves to 4-day running mean zonal wind data, averaged between 50-70°N. The planetary wave structure in PRISM closely follows that of NAVGEM-HA, which is marked by a PW1 enhancement leading up to the end of December, followed by a PW2 amplification in early January. This temporal evolution of the planetary wave structure is also consistent with earlier studies of the 2013 SSW event (Nath et al., 2016; Coy & Pawson, 2015; L. Goncharenko et al., 2013).

Below an altitude of 85 hPa, PRISM is nudged to daily mean winds and temperatures calculated from 1-hourly ECMWF ERA5 reanalysis data (Hersbach et al., 2020). Above 0.001 hPa, the model is nudged to daily mean wind and temperature fields calculated from the Horizontal Wind Model version 2014 (HWM14, Drob et al., 2015) and from the NRLMSISE-00 reference model (Picone et al., 2002), respectively. Diagnostic simulations where the boundaries between the different datasets of the composite atmosphere are artificially smoothed, find that any discontinuities between the datasets do not significantly effect the simulated SDT field.

2.2 Solar Forcing

The solar thermal SDT is forced by incorporating hourly global temperature tendency fields (TTFs) from the ECMWF Integrated Forecasting System (IFS) cycle 41r2 forecast model (Ehard et al., 2018). These TTFs include radiative and latent heating effects from the surface up to ∼80 km altitude, and are interpolated onto the PRISM model time-step. The ERA5 forecast model is initialized twice daily at 06:00 and 18:00 UTC based on a broad range of observations, and the 12 hr segments following each initialization are used

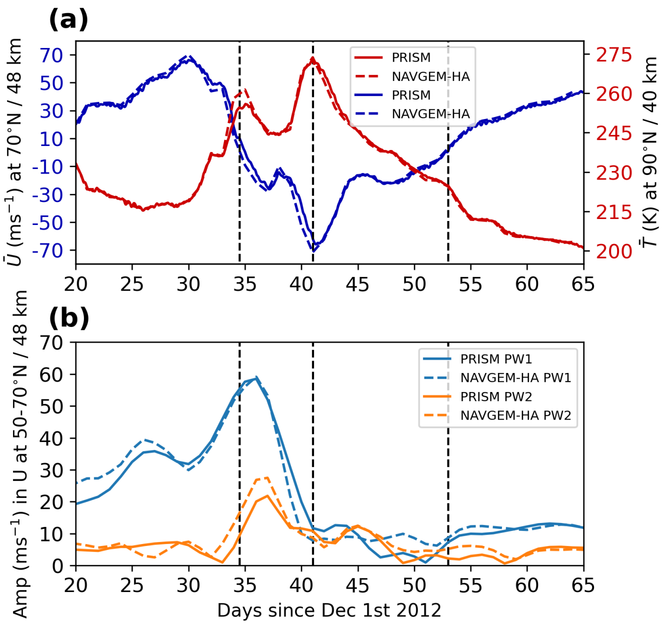

Figure 1. Panel **(a)** shows the time development of PVW as simulated by PRISM (solid lines) and by the NAVGEM-HA model (dotted lines). Panel **(b)** shows the corresponding time development of the PW1 and PW2 amplitudes in the zonal wind at 48 km altitude averaged between 50-70°N. The vertical dashed lines mark the SSW onset, peak PVW, and recovery dates as defined in Section 2.1.

to construct a continuous dataset of hourly TTFs. While the IFS TTFs extend only up to an altitude of ~80 km, the contribution to the simulated SDT by the tide forced above this altitude is very small compared to those forced in the tropospheric and stratospheric regions (van Caspel et al., 2022).

One limitation of the IFS TTFs is that its radiative transfer model does not include interactive ozone chemistry, but instead specifies a climatological zonal mean stratospheric ozone distribution (ECMWF, 2020). Consequently, the IFS TTFs cannot describe the thermal forcing changes caused by a redistribution of stratospheric ozone. In Section 4.2.1, this limitation is addressed by using 3-hourly TTFs from the Specified Dynamics Whole Atmosphere Community Climate Model with Thermosphere Extension version 2.1 (SD-WACCMX, H.-L. Liu et al., 2018). However, while the SD-WACCMX TTFs include interactive ozone chemistry, diagnostic simulations find that the short-term variability of the solar SDT forcing is better represented in the IFS forecast model.

2.3 Lunar Forcing

Following the approach of Pedatella et al. (2012), the lunar M_2 (12.42 hr) and N_2 (12.66 hr) SDT components are prescribed by including the momentum forcing arising from the horizontal gradient of the lunar tidal potentials. The tidal potential is described by its contributions arising from the lunar gravitational potentials (Ω), the vertical displacement of the ocean, load, and solid Earth tides ($g\zeta$, where g = 9.81 ms^{-1} and ζ is the vertical displacement in meters), and the tidally induced redistribution of solid Earth mass (Ω^e). The potential arising from the tidally induced redistribution of ocean mass represents only a very minor contribution (Vial & Forbes, 1994), and is ignored in this work.

The lunar gravitational potentials are described by

$$\begin{aligned}\Omega_{M_2} &= -0.7933 P_2^2(\theta)\cos(2\tau)\\ \Omega_{N_2} &= -0.1518 P_2^2(\theta)\cos(2\tau - s + p)\end{aligned}$$

in units of $\mathrm{m^2 s^{-2}}$, where $P_2^2(\theta) = 3\sin^2\theta$ is an associated Legendre polynomial and θ is co-latitude (Chapman & Lindzen, 1970). In the above time factors, $\tau = t + h - s$ where h, s, and p are given by

$$\begin{aligned}h &= 279.69668 + 36000.76892T + 0.00030T^2\\ s &= -270.43659 + 481267.89057T + 0.00198T^2\\ p &= 334.32956 + 4069.03403T - 0.01032T^2 - 0.00001T^3\end{aligned}$$

in units of degrees. Here T represents the time since Greenwich mean noon on 1899 December 31 (epoch 1900) in units of a Julian century (36525 days), and t is the angular measure of mean solar time ($15° = 1$ hr). The M_2 potential describes the classic double tidal bulge, while the N_2 potential describes the $\sim 20\%$ amplitude variations of the M_2 potential caused by the ellipticity of the lunar orbit.

The Earth tide accounts for the vertical displacement of the Earth's crust in response to the lunar gravitational field. Furthermore, the Earth tide is accompanied by a geopotential perturbation arising from the associated redistribution of crustal mass. Both the Earth tide and the associated mass-redistribution potentials can be expressed as Love-number multiplications of the lunar gravitational potentials, where the Love numbers are given by $h_2 = -0.609$ and $k_2 = 0.302$, respectively (Hollingsworth, 1971). The M_2 and N_2 Earth tide potential can then be written as $(\zeta^e_{M_2} + \zeta^e_{N_2})g = h_2(\Omega_{M_2} + \Omega_{N_2})$, and the associated mass-redistribution potential as $\Omega^e_{M_2} + \Omega^e_{N_2} = k_2(\Omega_{M_2} + \Omega_{N_2})$.

To force the lunar ocean and load tide components, hourly M_2 and N_2 elevation fields from the FES2014 ocean tide atlas are incorporated. The FES2014 model combines the hydrodynamic modeling of the ocean tides with ensemble data assimilation techniques, providing global instantaneous ocean and load tide elevation fields (Lyard et al., 2021). While the ocean tide represents the vertical displacement of the ocean surface, the load tide represents the vertical displacement of the ocean crust in response to the loading by the ocean tides.

To verify the implementation of the lunar tide forcing, migrating lunar SDT (lunar SW2, for Semidiurnal, Westward S = 2) simulations are compared against climatological simulations from the Global Scale Wave Model (GSWM) and Whole-Atmosphere Community Climate Model (WACCM), as described in detail in Pedatella et al. (2012). While the GSWM and WACCM simulations do not include the N_2 tidal potentials, these tidal components have very little impact on the monthly mean amplitudes discussed in the following. For the PRISM lunar validation simulation, the lunar tide forcing for the year 2013 is propagated through a climatological background atmosphere based on monthly mean zonal mean zonal winds and temperatures from the upper atmosphere research satellite (UARS) reference atmosphere project (URAP, Swinbank & Ortland, 2003). The URAP atmosphere extends from the surface up to ~110 km altitude, and is padded to HWM14 and MSISE-00 fields for altitudes above that. No thermal forcing is included in the lunar validation simulation, such that the amplitude of the lunar SW2 can easily be extracted using 4-day sliding window Fourier analysis.

Fig. 2 shows the simulated mean January and June lunar SW2 amplitudes in the zonal winds. The vertical and latitudinal tidal structure follows those simulated by the GSWM and WACCM models, as shown in Pedatella et al. (2012), with peak amplitudes occurring in the summer hemisphere between 40-50° latitude and 110-125 km altitude. Amplitudes in the winter hemisphere are around a factor of two smaller, and maximize roughly between 100-120 km. We note that, while Pedatella et al. (2012) find that GSWM lunar amplitudes

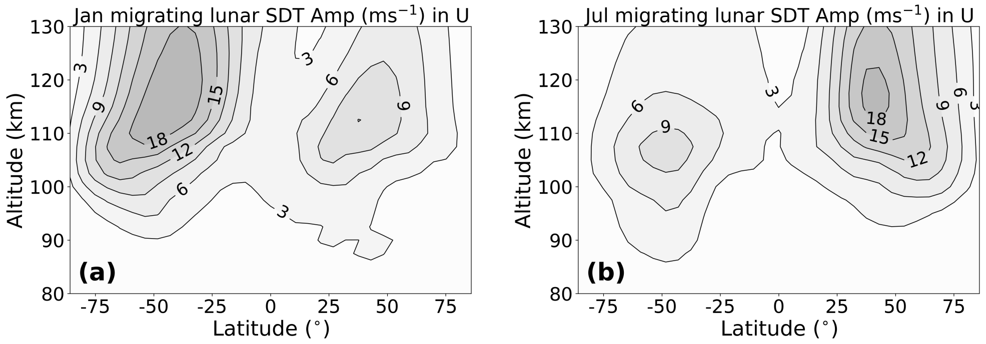

Figure 2. Monthly mean lunar SW2 amplitude in the zonal winds simulated by the climatological PRISM lunar tide simulation for January **(a)** and July **(b)**.

are a factor of 2-3 greater than those simulated by WACCM, the magnitude of the amplitudes simulated by PRISM more closely agree with those of the GSWM. For example, peak amplitudes in January are around 18 ms^{-1} in PRISM, 8 ms^{-1} in WACCM, and 22 ms^{-1} in GSWM.

3 Comparison to Observations

In this section, the simulated SDT response is compared against meteor wind observations from the CMOR, Collm, and Kiruna meteor radar sites. The relative importance of the solar and lunar SDT components is quantified by comparison against individual lunar and solar SDT simulations. We note that the results presented in this section do not depend on the choice of zonal or meridional winds, and therefore only the zonal component is discussed.

3.1 SDT Response

The CMOR, Collm, and Kiruna meteor radars provide hourly horizontal winds by measuring the so-called meteor trail position data (Hocking et al., 2001), with details of the radars and wind retrieval algorithm given by Stober et al. (2022, 2021). We note that the Collm meteor radar received an upgrade in 2015, with the 2012/2013 configuration described in more detail by Jacobi et al. (2007). In the current work, meteor radar wind measurements between 80-97 km altitude are used, having vertical resolutions between 2-3 km. To extract the SDT amplitude and phase from the hourly winds, a least-squares 4-day sliding window fit of a mean and sine waves representing the diurnal, semidiurnal and terdiurnal tides is performed. Here the fitted SDT includes only a 12.00 hr wave, since the employed 4-day time window effectively aliases the solar and lunar SDT components. To compare the model to observation, hourly PRISM output is interpolated to the geographic locations of the meteor radars, and analyzed using the same least-squares fitting routine.

Fig. 3 shows the measured and simulated amplitude of the SDT at the three radar sites. At the CMOR site (Fig. 3a and 3d), both the model and observations show a pronounced amplitude enhancement occurring roughly five days after peak PVW, with amplitudes reaching up to 70 ms^{-1}. This enhancement is preceded by a 10-day amplitude minimum of around 10-20 ms^{-1}, starting around the time of the SSW onset. Notably, a quasi 10-day periodicity is discernible in both the observed and simulated amplitudes, reaching local amplitude maxima around days 24, 31, 46, and 60. This periodicity is also observable at the CMOR and Kiruna sites, and will be discussed in more detail in Section 4.

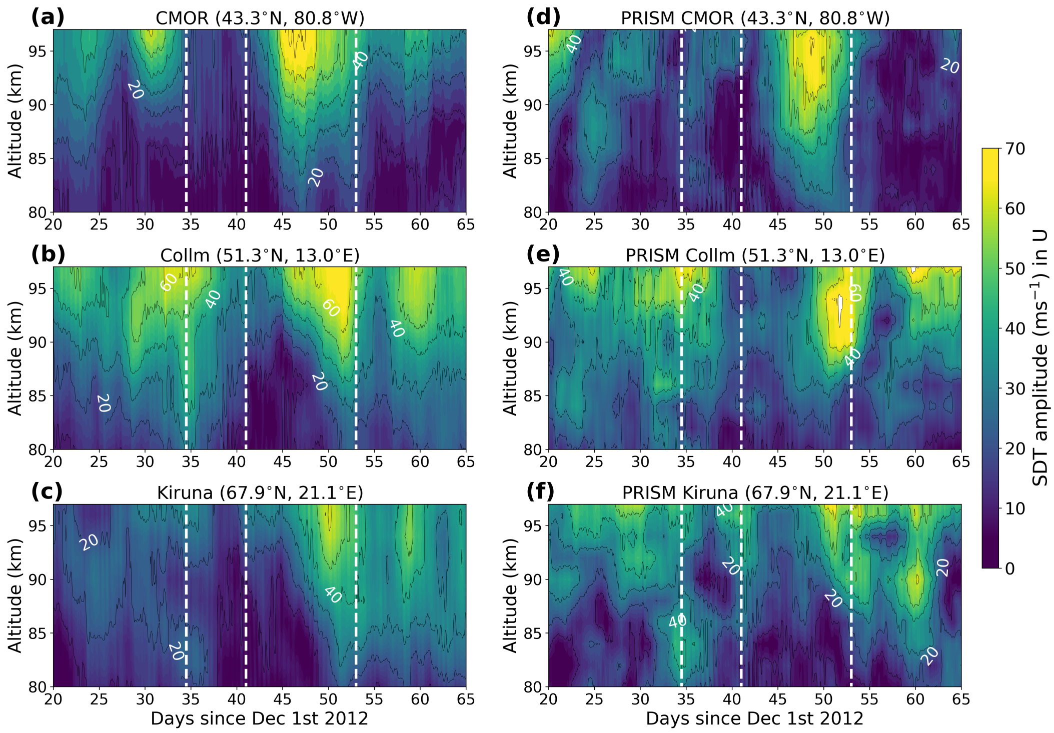

Figure 3. Comparison of the zonal SDT amplitude measured and simulated at the CMOR **(a,d)**, Collm **(b,e)**, and Kiruna **(c,f)** radar sites. Contours are spaced in 10 ms^{-1} intervals. The vertical dashed lines mark the SSW onset, peak PVW, and recovery onset as defined in Section 2.1.

At the Collm site (Fig. 3b and 3e), the observed and simulated SDT also show an amplitude enhancement with 60-70 ms^{-1} maximum, although here peak amplitudes occur nearer to 10 days after peak PVW. Similar to the CMOR site, the SDT enhancement is preceded by a ~10-day amplitude minimum. At the Kiruna site (Fig. 3c and 3f), the simulated and observed SDT is similar to the other sites, reaching peak amplitudes in the range of 50-60 ms^{-1} around 10 days after peak PVW. Here the preceding amplitude minimum is less pronounced, however, as amplitudes leading up to the onset date are comparatively smaller. The model also shows more variability in the vertical compared to observation, while amplitudes are overestimated by around 20 ms $^{-1}$ between days 20 and 40.

Fig. 4 shows the phase of the simulated and observed SDT at the three radar sites, expressed here in terms of the Local Time Of Maximum (LTOM). The local time at each radar site is calculated as $t_{local} = t_{UTC} + 24 \cdot \lambda/360$, where λ is the station longitude in degrees. The observed phase displays similar characteristics at all three radar sites, where the LTOM shifts to an earlier time by about 3-4 hr over the course of a five day period following peak PVW. While this behavior is reproduced by the model at all three sites, the simulated phase shift is instead nearer to 2-3 hr. In addition, the simulated phase at the Kiruna site is overestimated by about 2 hrs on average, while the phase at the CMOR site displays more variability than observation between days 50 and 65.

3.2 Solar and Lunar SDT Response

Numerical experiments are performed to investigate the individual contributions of the lunar and solar SDT components to the total simulated SDT. This is achieved by performing simulations where only the lunar SDT forcing (OnlyLunar) or only the thermal forcing

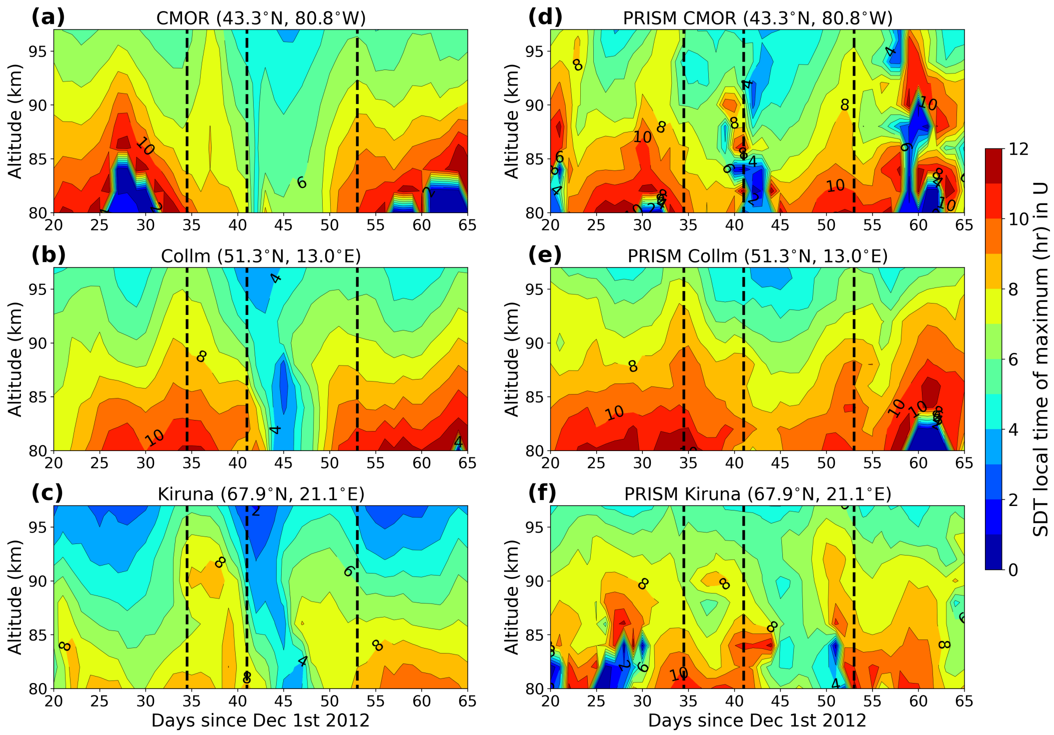

Figure 4. Comparison of the zonal SDT phase (LTOM) simulated by PRISM and measured by the CMOR **(a,d)**, Collm **(b,e)**, and Kiruna **(c,f)** meteor radars. Contours are spaced in 1 hr intervals. The vertical dashed lines mark the SSW onset, peak PVW, and recovery onset as defined in Section 2.1.

(OnlySolar) are included. Fig. 5 compares the two simulations, where the solar SDT is denoted by S_2 and the lunar SDT by M_2. As before, the tidal amplitudes are calculated using a 4-day sliding window, but now the least-squares fit to the OnlyLunar simulation uses a 12.42 hr wave rather than a 12.00 hr wave (although the results are very similar using either a 12.00 hr or 12.42 hr wave period). Fig. 5a-c shows that the simulated solar SDT closely resembles that of the full PRISM simulation (shown in Fig. 3d-f). The most notable differences with the full PRISM simulation are that the amplitude enhancements following peak PVW are 5-10 ms^{-1} lower, while the amplitude minima preceding the enhancements are 5-10 ms^{-1} higher.

Fig. 5d-f shows that the lunar SDT enhances broadly between peak PVW and the recovery phase onset, reaching amplitudes between 12-14 ms^{-1} at all three radar sites. The magnitude of the lunar SDT amplitude is only around 15-20% of that of the solar SDT at the time of the enhancement. Furthermore, a diagnostic simulation without the lunar N_2 forcing included shows difference of less than 3 ms^{-1} with the OnlyLunar simulation, indicating that there is no particular enhancement of the N_2 component taking place. In agreement with lunar amplitudes being considerably smaller than the solar component, diagnostic analysis finds that the phase behavior of the SDT over the course of the SSW closely follows that of the solar component.

It is important to note that the OnlySolar and OnlyLunar simulations cannot capture the effects of any wave-wave interactions between the solar and lunar SDT components. However, diagnostic analysis finds that the sum of the OnlySolar and OnlyLunar simulations closely matches that of the PRISM simulation, suggesting that tidal wave-wave interactions

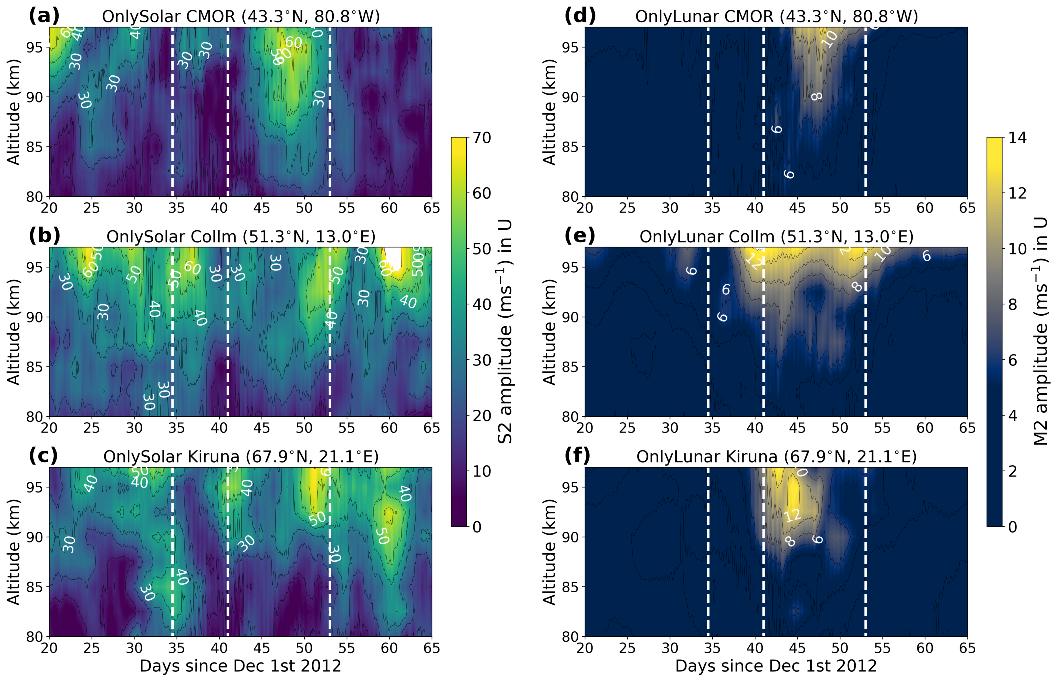

Figure 5. Comparison of the zonal SDT amplitude simulated by the OnlySolar and OnlyLunar simulations at the CMOR **(a,d)**, Collm **(b,e)**, and Kiruna **(c,f)** sites. Contours are spaced in 10 ms^{-1} intervals for the left-hand panels, and 4 ms^{-1} intervals for the right-hand panels. The vertical dashed lines mark the SSW onset, peak PVW, and recovery onset as defined in Section 2.1.

are limited. We note that differences between the sum of the OnlySolar and OnlyLunar simulations and the full PRISM simulation can also arise from a certain degree of internal variability, or noise, present from simulation to simulation. This noise can lead to SDT amplitude variations on the order of a few ms^{-1}, which we attribute to internal gravity wave variability.

4 Model Analysis

Further numerical experiments are performed to quantify the individual contributions to the simulated SDT response of the changing propagation conditions through the zonal mean background atmosphere, non-linear wave-wave interactions with quasi-stationary planetary waves, and thermal forcing variations caused by a stratospheric ozone redistribution. An overview of the experiments of this section is given in Table 1.

4.1 Migrating and Non-Migrating SDT Response

To gain insight into the drivers of the SDT response, the simulated tidal wave field is decomposed into its migrating and non-migrating components. These tidal components are calculated by performing a 4-day sliding window 2-D Fourier decomposition of the simulated zonal wind field. In the simulation results, the two gravest non-migrating components are found to be the westward zonal wavenumber S = 1 (SW1) and westward zonal wavenumber S = 3 (SW3) tides (consistent with the results of Stober et al. (2020)), which can be produced by the interaction between the migrating SDT (SW2) and quasi-stationary PW1 waves (Angelats i Coll & Forbes, 2002; Teitelbaum & Vial, 1991). Non-migrating tides other than these two components are not discussed here.

Table 1. Numerical experiment model setup.

Experiment	Configuration
PRISM	Model configuration as described in Section 2
OnlyLunar	As PRISM, only lunar SDT forcing
OnlySolar	As PRISM, only solar SDT forcing
FixedAtmos	As OnlySolar, atmosphere fixed to zonal mean Dec 20th 2012
FixedForcing	As OnlySolar, forcing includes only SW2 fixed to Dec 20th 2012
FixedForcingZM	As FixedForcing, no background planetary waves included
WACStrat	As OnlySolar, forcing only between 100-0.1 hPa based on SD-WACCMX

Fig. 6a-c shows the latitude-time development of the SW1, SW2, and SW3 amplitudes in the PRISM simulation at 97 km altitude, corresponding to the highest altitude of the Collm, CMOR, and Kiruna meteor wind measurements. However, the results are independent of the choice of altitude for the altitude range considered in this work. The SW1 tide reaches amplitudes up to 27 ms^{-1} both before and after peak PVW, though amplitudes are generally highest for the period between peak PVW and the recovery onset. The largest SW1 tide amplitudes are, however, contained to latitudes above 50°N. Fig. 6b illustrates that the largest amplitudes occur in the SW2 component, consistent with the results of Hibbins et al. (2019). One notable feature of the SW2 tide is that its amplitudes are reduced by 20-30 ms^{-1} during a 10-day period centered roughly on the day of peak PVW. Furthermore, while the SW2 tide generally peaks between 50-70°N, its amplitude is increased between days 43-48 around 30-45°N, corresponding to the latitude band of the CMOR radar. SW2 amplitudes nevertheless stay below 45 ms^{-1} at all latitudes up until day 60. For the SW3 tide, amplitudes intermittently reach values between 10-20 ms^{-1} both before, after, and during the SSW.

In Fig. 6, the horizontal lines mark the latitudes of the meteor radars. Tracing, for example, the latitude of the Kiruna radar, shows that around the time of the peak amplitude enhancement (day 50, reaching up to 60 ms^{-1}), nearly half of the local amplitude is the result of the constructive interference between non-migrating tides and the SW2 tide. Similarly, over half of the peak amplitude of 70 ms^{-1} at the CMOR radar is the result of non-migrating tides, as SW2 amplitudes reach only up to around 30 ms^{-1} around that time.

In Fig. 6d-f the latitude-time development of the SW1, SW2, and SW3 tides in the OnlySolar simulation are shown. The close correspondence between these results and those of the PRISM simulation reaffirm the minimal role of the lunar SDT at these altitudes. Therefore, in the following investigation of the driving mechanisms of the SDT response, only the solar tidal components are considered.

4.2 Forcing Mechanisms

To isolate the impact of variations in the thermal forcing, the background atmosphere in the FixedAtmos experiment is fixed to that of the 20th December 2012, representing pre-SSW conditions. In addition, no planetary waves are included, such that any variations in the simulated non-migrating tides are caused by variations in the thermal forcing itself. Excluding the planetary waves is achieved by nudging the wave field towards zero rather than the daily mean NAVGEM-HA fields. Fig. 7a-c shows the resulting latitude-time development of the SW1, SW2, and SW3 tidal amplitudes. At the meteor radar latitudes, SW1 amplitudes remain mostly below 5 ms^{-1}, but reach up to 10 ms^{-1} around day 60. Fig. 7b shows that the resulting SW2 tide is marked by a quasi 10-day periodicity, having variations on the order of 10-20 ms^{-1}. This periodicity is also observed in the PRISM and OnlySolar

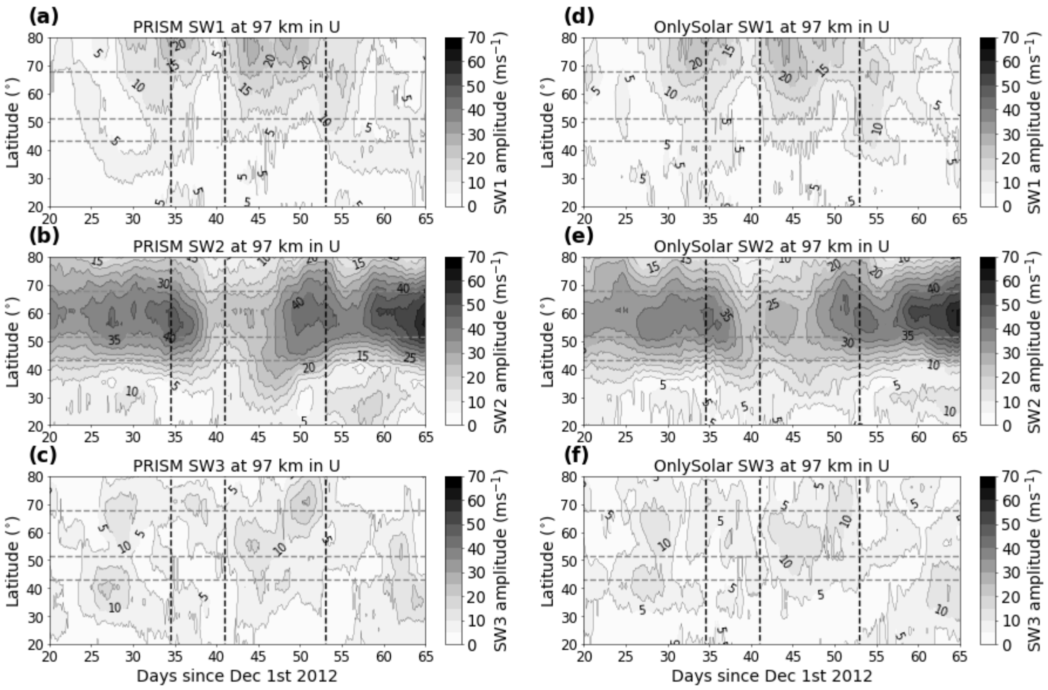

Figure 6. Latitude-time development of the zonal SW1, SW2, and SW3 amplitudes at 97 km altitude from the PRISM **(a,b,c)** and OnlySolar **(d,e,f)** simulations. The vertical dashed lines mark the SSW onset, peak PVW, and recovery onset as defined in Section 2.1. The horizontal dashed lines mark the latitudes of the three meteor radars used in this study.

simulations at the CMOR, Collm, and Kiruna meteor radar sites, as discussed in Section 3. Note that these variations are the results of variations in the tropospheric forcing, as the stratospheric forcing is based on a climatological ozone distribution. The SW3 tide shown in Fig. 7c reaches amplitudes of up to 12 ms^{-1} throughout the mid- and high-latitudes.

Fig. 7d-f shows the latitude-time development of the SW1, SW2, and SW3 amplitudes from the FixedForcing experiment. The FixedForcing experiment employs a thermal forcing fixed to that of the 20th of December, while the background atmospheric variations are as in the full PRISM simulation. In addition, only the dominant SW2 forcing component is included, such that any non-migrating tides are the result of wave-wave interactions. The resulting SW1 tide closely resembles that of the OnlySolar simulation, reaching amplitudes of up to 24 ms^{-1} around day 45. The SW2 tide also displays similar characteristics to that of the OnlySolar simulation (Fig. 6d), with a 10-day amplitude minimum broadly centered on the day of peak PVW. The SW2 also shows a maximum around day 35, and a broad maximum after day 55. For the SW3 tide, the FixedForcing experiment identifies a pronounced non-linear wave-wave forcing occurring around day 45 between 50-60°N, reaching amplitudes of up to 18 ms^{-1}. However, since the thermal variations of the SW3 tide are similar in magnitude to those from the FixedForcing experiment, the wave-wave forcing response is difficult to uniquely separate from the full PRISM and OnlySolar simulations.

To isolate the impact of the changing propagation conditions through the zonal mean background atmosphere, the FixedForcingZM experiment repeats the FixedForcing experiment, but without the inclusion of planetary waves. Any variations in the SW2 amplitudes are then the result of variations in the zonal mean propagation conditions. Fig. 8 shows that the resulting SW2 follows that of the FixedForcing experiment, although amplitudes are generally higher at times when large non-migrating tides are present in the FixedForcing

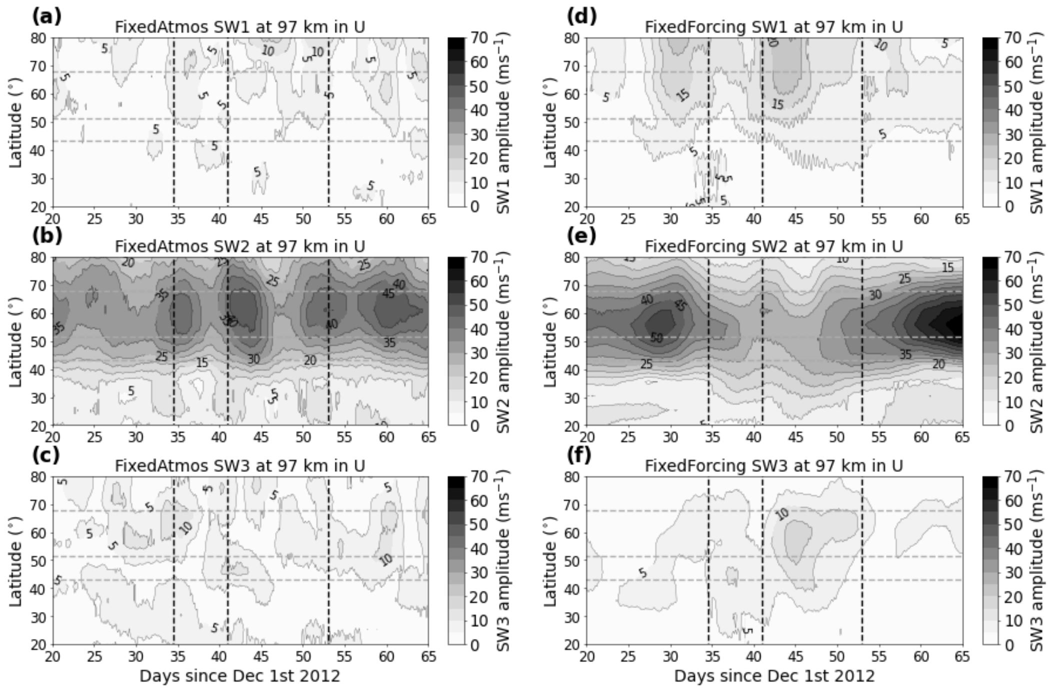

Figure 7. Latitude-time development of the zonal SW1, SW2, and SW3 amplitude at 97 km altitude for the FixedAtmos **(a,b,c)** and FixedForcing **(d,e,f)** experiments listed in Table 1. The vertical dashed lines mark the SSW onset, peak PVW, and recovery onset as defined in Section 2.1. The horizontal dashed lines mark the latitudes of the three meteor radars used in this study.

experiment (i.e., when the SW2 interacts with planetary waves). Nevertheless, the characteristic amplitude minimum centered roughly on the day of peak PVW is reproduced, along with the amplitude maxima around day 30 and after day 55.

4.2.1 Stratospheric Ozone

As discussed in Section 2, the employed IFS TTFs can not be used to describe the effects of a SSW-induced stratospheric ozone redistribution on the thermal SDT forcing. To determine the importance of this effect, a simulation is performed using 3-hourly TTFs from the SD-WACCMX model. The SD-WACCMX model includes parameterizations of all the major chemical and radiative processes from the surface to the thermosphere, and incorporates the instantaneous modeled stratospheric ozone distribution in its radiative transfer calculations. The model also captures the dynamics of the 2013 SSW, by virtue of its assimilated MERRA-2 reanalysis winds and temperatures for altitudes below ∼50 km.

To illustrate the effect of the SSW on the stratospheric ozone distribution, Fig. 9a shows the SD-WACCMX ozone mixing ratios at 40 km altitude on the day of peak PVW. Here a zonal wavenumber S = 1 structure is visible in the ozone mixing ratios between 40-50°N, which is shaped by the zonally asymmetric transport of ozone in response to the SSW. To isolate the impact of the ozone redistribution on the thermal SDT forcing, the WACStrat experiment includes only the SD-WACCMX TTFs between 100-0.1 hPa (10-70 km altitude), spanning the entire stratospheric ozone forcing region (van Caspel et al., 2022). Similar to the FixedAtmos experiment, the specified winds and temperatures of the background atmosphere are fixed to that of the 20th of December 2012 and include

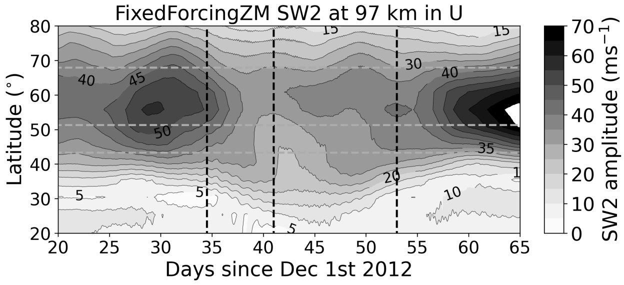

Figure 8. Latitude-time development of the zonal SW2 amplitude at 97 km altitude for the FixedForcingZM experiment listed in Table 1. The vertical dashed lines mark the SSW onset, peak PVW, and recovery onset as defined in Section 2.1. The horizontal dashed lines mark the latitudes of the three meteor radars used in this study.

no planetary waves. Any variations in the migrating and non-migrating tides can then be attributed to variations in the stratospheric ozone forcing itself.

Fig. 9b-d shows the time evolution of the SW1, SW2, and SW3 tidal amplitudes. The amplitude of the SW2 forcing response is decreased by 3-4 ms^{-1} about five days after peak PVW, while the SW1 component peaks at 2 ms^{-1} five days before peak PVW at 65°N. The largest variations occur in the SW3 component, which reaches amplitudes of up to 4-5 ms^{-1} five days before peak PVW at 50°N.

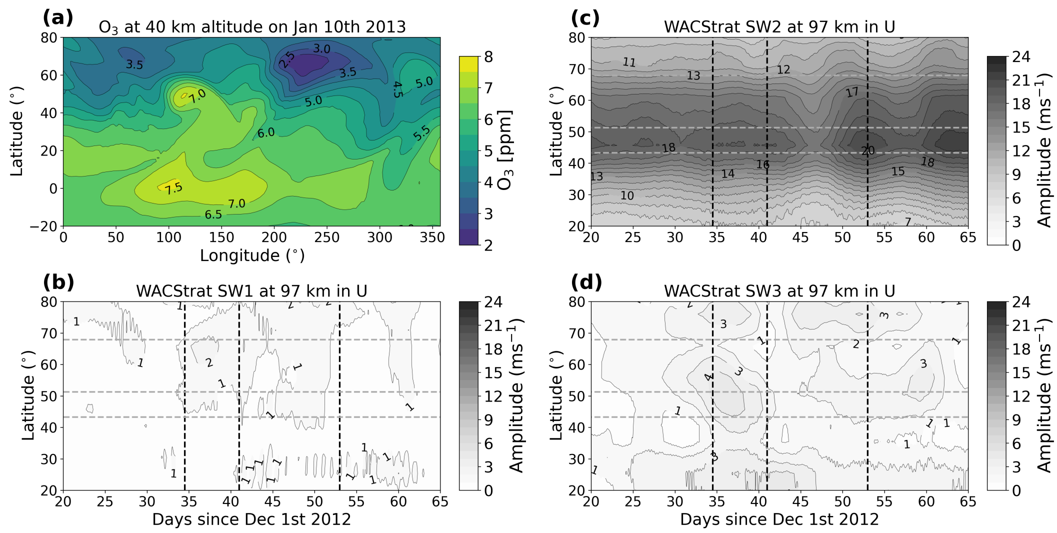

Figure 9. SD-WACCMX ozone mixing ratios at 40 km altitude on the 11th of January 2013 **(a)**, and the latitude-time development of the zonal SW1 **(b)**, SW2 **(c)**, and SW3 **(d)** amplitudes at 97 km altitude from the WACStrat experiment. Contours for the tidal amplitudes are spaced in 1 ms^{-1} intervals. The vertical dashed lines mark the SSW onset, peak PVW, and recovery onset as defined in Section 2.1. The horizontal dashed lines mark the latitudes of the three meteor radars used in this study.

5 Discussion and Conclusion

In this study, the SDT response to the 2013 SSW is simulated using the mechanistic PRISM tidal model. The model includes a detailed description of the lunar and solar tidal forcing terms, and the tides are propagated through a realistic background atmosphere based on the NAVGEM-HA meteorological analysis system. The simulated amplitude and phase variability of the SDT are found to be in close agreement with measurements made at the CMOR (43.3°N, 80.8°W), Collm (51.3°N, 13.0°E), and Kiruna (67.5°N, 20.1°E) radar sites between 80-97 km altitude. The SDT response is characterized by a 10-day amplitude minimum, followed by a 60-70 ms^{-1} amplitude maximum 5-10 days after peak PVW.

Numerical experiments where only the solar or lunar tidal forcing terms are included, find that the net simulated SDT response closely follows that of the solar component. During the time of the SDT enhancement, lunar amplitudes are around 10-15% of that of the solar component, reaching amplitudes of up to 12-14 ms^{-1} over the course of the SSW. Further numerical experiments find that the response of the solar SDT is governed by the changing zonal mean propagation conditions through the background atmosphere, and by non-linear wave-wave interactions between the SW2 tide and quasi-stationary planetary waves. The zonal mean propagation conditions shape the observed 10-day amplitude minimum, while non-migrating tides can contribute up to 50% of the net SDT amplitude during the enhancement following peak PVW. The impact of the SSW-induced redistribution of stratospheric ozone is found to be small, inducing amplitude variations of only up to 4 ms^{-1}.

In our results, the minimal role of the lunar SDT contrasts earlier reports of a strongly enhanced lunar SDT during the 2013 SSW, and during SSWs in general (e.g., Koushik et al., 2020; Conte et al., 2017; Chau et al., 2015; Xiong et al., 2013). We suggest that this discrepancy can be explained by the inherent difficulty of separating the solar and lunar SDT frequencies over the course of a SSW event. By way of illustration, the commonly used method of a 16-day sliding window fit containing both the 12.00 hr (solar) and 12.42 hr (lunar) SDT components is demonstrated, using the observed and simulated zonal winds at the CMOR radar site. The following results, however, also apply to window lengths anywhere between 14 to 21 days.

Fig. 10a,d shows the 16-day sliding window solar and lunar SDT amplitudes from the observed CMOR winds. The qualitative behavior of both tidal components follows that of the net observed SDT (Fig. 3a), showing strongly enhanced amplitudes around 5-10 days following peak PVW. Peak lunar amplitudes reach up to $\sim$24 ms^{-1}, and are nearly half that of the peak solar amplitudes. Applying the 16-sliding window fit to the CMOR winds simulated by PRISM shows similar results (Fig. 10b,e). The lunar amplitudes calculated for the PRISM simulation strongly contrast the results from Section 3.2, however, where the individual lunar tide simulation found amplitudes no greater than 14 ms^{-1}. That the high amplitudes calculated from the 16-day sliding window fit are instead caused by cross-contamination effects with the solar SDT, is illustrated in Fig. 10c,f. Here the 16-day sliding window analysis is applied to a simulation without a lunar tide forcing (OnlySolar). However, the same qualitative response for both the lunar and solar SDT components is reproduced, with lunar SDT amplitudes of up to 24 ms^{-1}. Similar analysis finds that the OnlySolar simulation yields cross-contaminated lunar SDT amplitudes of up to 24 ms^{-1} and 16 ms^{-1} at the Collm and Kiruna sites, respectively.

Diagnostic analysis where the 16-day sliding window fit is applied to the results from a simulation including only the thermal forcing and a fixed background atmosphere (FixedAtmos), find no evidence of lunar tide periodicities in the thermal forcing itself. It also finds no evidence of a (contaminated) lunar SDT response to the SSW. Applying the 16-day fit to a simulation with a fixed daily thermal forcing (FixedForcing) does, however, closely reproduce the cross-contaminated lunar tide enhancement. Thus indicating that the cross-contamination of the lunar SDT is caused by the SSW-induced variability in the propagation conditions of the solar SDT component. For example, the phase variation of the solar SDT over the 16 day window translates to a transient frequency variation. This in turn results in the bleeding of the 12.00 hr solar tide into the lunar spectral bandwidth.

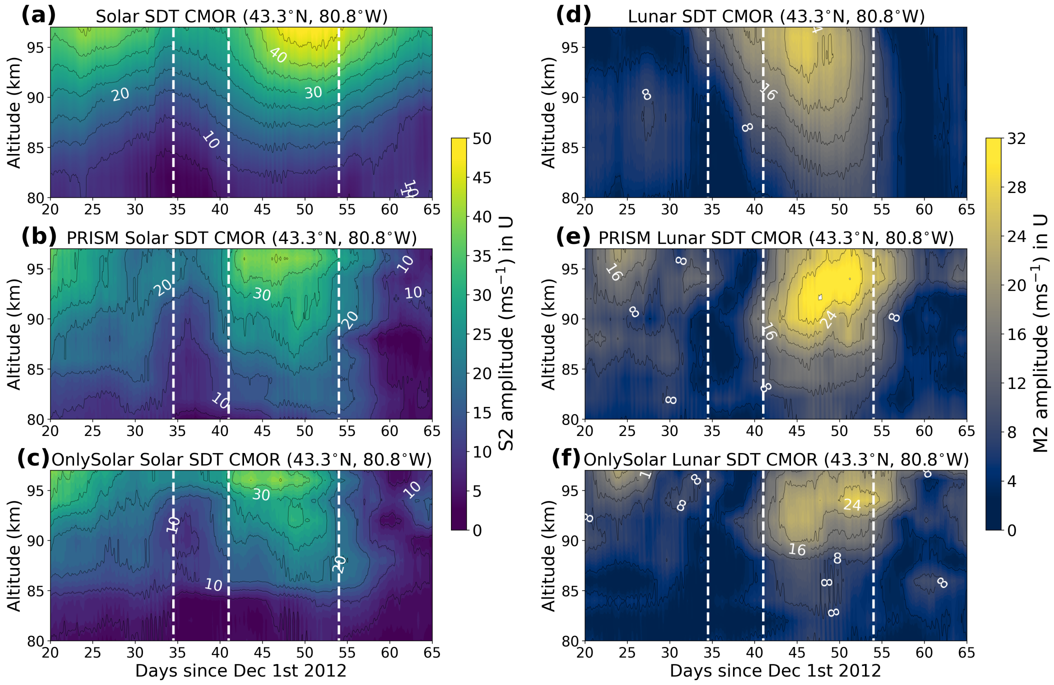

Figure 10. Solar and lunar SDT zonal amplitude calculated using a 16-day sliding window for the CMOR meteor winds **(a,d)**, PRISM simulation **(b,e)**, and OnlySolar experiment **(c,f)**. Note the different color scaling for the left-hand and right-hand panels. The vertical dashed lines mark the SSW onset, peak PVW, and recovery onset as defined in Section 2.1.

In summary, the SDT response to the 2013 SSW is found to be governed by that of the solar SDT component. This response is driven by the changing propagation conditions through the background atmosphere and by non-linear wave-wave interactions with quasi-stationary planetary waves. Non-migrating tides can contribute up to half of the net SDT response, suggesting that the SDT response at any given geographical location strongly depends on the planetary wave structure of the SSW. A climatological analysis of the SDT response at any location is therefore anticipated to require the sampling of a large number of events. In addition, the study of the SDT response is further complicated by the short-term variability of the solar component easily leading to an overestimation of the lunar amplitudes when both are separated over the course of a SSW. Future work will go out to studying the SDT response to other SSWs using the methodology outlined in this work, while also extending the analysis to other altitude regions.

Acknowledgments

The current research was supported by the Research Council of Norway (grant no. 223525/F50). The authors acknowledge the use of NAVGEM-HA data. Development of NAVGEM-HA was supported by the Chief of Naval Research and the Department of Defense High Performance Computing Modernization Project. CL acknowledges support by Deutsche Forschungsgemeinschaft (grant no. JA836/47-1).

Hourly ERA5 model level forecast data are available through the climate data store (CDS, `https://cds.climate.copernicus.eu`). SD-WACCMX data are available from `https://www.earthsystemgrid.org` CCSM run SD-WACCM-X v2.1, Atmosphere History Data, 3-Hourly Instantaneous Values, version 7.

The code used to compute FES2014 was developed in collaboration between Legos, Noveltis, CLS Space Oceanography Division and CNES, and is available under GNU General Public License.

The Esrange meteor radar operation, maintenance and data collection is provided by Esrange Space Center of Swedish Space Corporation.

This work was supported in part by the NASA Meteoroid Environment Office under cooperative agreement 80NSSC21M0073.

References

Angelats i Coll, M., & Forbes, J. M. (2002). Nonlinear interactions in the upper atmosphere: The s = 1 and s = 3 nonmigrating semidiurnal tides. *Journal of Geophysical Research: Space Physics*, *107*(A8), SIA 3-1-SIA 3-15. doi: https://doi.org/10.1029/2001JA900179

Arras, C., Jacobi, C., & Wickert, J. (2009). Semidiurnal tidal signature in sporadic e occurrence rates derived from gps radio occultation measurements at higher midlatitudes. *Annales Geophysicae*, *27*(6), 2555–2563. doi: 10.5194/angeo-27-2555-2009

Baldwin, M. P., Ayarzagüena, B., Birner, T., Butchart, N., Butler, A. H., Charlton-Perez, A. J., ... Pedatella, N. M. (2021). Sudden stratospheric warmings. *Reviews of Geophysics*, *59*(1), e2020RG000708. doi: 10.1029/2020RG000708

Chapman, S., & Lindzen, R. S. (1970). *Atmospheric tides*. Springer Netherlands. doi: https://doi.org/10.1007/978-94-010-3399-2

Charney, J. G., & Drazin, P. G. (1961). Propagation of planetary-scale disturbances from the lower into the upper atmosphere. *Journal of Geophysical Research (1896-1977)*, *66*(1), 83-109. doi: https://doi.org/10.1029/JZ066i001p00083

Chau, J. L., Hoffmann, P., Pedatella, N. M., Matthias, V., & Stober, G. (2015). Upper mesospheric lunar tides over middle and high latitudes during sudden stratospheric warming events. *Journal of Geophysical Research: Space Physics*, *120*(4), 3084-3096. doi: 10.1002/2015JA020998

Conte, J. F., Chau, J. L., Stober, G., Pedatella, N., Maute, A., Hoffmann, P., ... Murphy, D. J. (2017). Climatology of semidiurnal lunar and solar tides at middle and high latitudes: Interhemispheric comparison. *Journal of Geophysical Research: Space Physics*, *122*(7), 7750-7760. doi: https://doi.org/10.1002/2017JA024396

Coy, L., & Pawson, S. (2015, feb). The major stratospheric sudden warming of january 2013: Analyses and forecasts in the GEOS-5 data assimilation system. *Monthly Weather Review*, *143*(2), 491–510. doi: 10.1175/mwr-d-14-00023.1

Drob, D. P., Emmert, J. T., Meriwether, J. W., Makela, J. J., Doornbos, E., Conde, M., ... Klenzing, J. H. (2015). An update to the horizontal wind model (HWM): The quiet time thermosphere. *Earth and Space Science*, *2*(7), 301–319. doi: https://doi.org/10.1002/2014ea000089

ECMWF. (2020). Ifs documentation cy47r1 - part iv: Physical processes. In *Ifs documentation cy47r1.* doi: 10.21957/cpmkqvhja

Ehard, B., Malardel, S., Dörnbrack, A., Kaifler, B., Kaifler, N., & Wedi, N. (2018). Comparing ecmwf high-resolution analyses with lidar temperature measurements in the middle atmosphere. *Quarterly Journal of the Royal Meteorological Society*, *144*(712), 633–640. doi: 10.1002/qj.3206

Forbes, J. M. (2009). Vertical coupling by the semidiurnal tide in earth's atmosphere. *In T. Tsuda, R. Fujii, K. Shibata, & M. A. Geller (Eds.), Climate and Weather of the Sun-Earth System(CAWSES): Selected Papers from the 2007 Kyoto Symposium(pp.*

337–348). Tokyo: TERRAPUB.

Forbes, J. M., & Zhang, X. (2012). Lunar tide amplification during the january 2009 stratosphere warming event: Observations and theory. *Journal of Geophysical Research: Space Physics*, *117*(A12). doi: https://doi.org/10.1029/2012JA017963

Goncharenko, L., Chau, J. L., Condor, P., Coster, A., & Benkevitch, L. (2013). Ionospheric effects of sudden stratospheric warming during moderate-to-high solar activity: Case study of january 2013. *Geophysical Research Letters*, *40*(19), 4982-4986. doi: 10.1002/grl.50980

Goncharenko, L. P., Coster, A. J., Plumb, R. A., & Domeisen, D. I. V. (2012). The potential role of stratospheric ozone in the stratosphere-ionosphere coupling during stratospheric warmings. *Geophysical Research Letters*, *39*(8). doi: https://doi.org/10.1029/2012GL051261

Goncharenko, L. P., Harvey, V. L., Liu, H., & Pedatella, N. M. (2021). Sudden stratospheric warming impacts on the ionosphere–thermosphere system. In *Ionosphere dynamics and applications* (p. 369-400). American Geophysical Union (AGU). doi: https://doi.org/10.1002/9781119815617.ch16

Goncharenko, L. P., Harvey, V. L., Randall, C. E., Coster, A. J., Zhang, S.-R., Zalizovski, A., ... Spraggs, M. (2022). Observations of pole-to-pole, stratosphere-to-ionosphere connection. *Frontiers in Astronomy and Space Sciences*, *8*. doi: 10.3389/fspas.2021.768629

Hagan, M. E. (1996, sep). Comparative effects of migrating solar sources on tidal signatures in the middle and upper atmosphere. *Journal of Geophysical Research: Atmospheres*, *101*(D16), 21213–21222. doi: https://doi.org/10.1029/96jd01374

Hersbach, H., Bell, B., Berrisford, P., Hirahara, S., Horányi, A., Muñoz-Sabater, J., ... others (2020). The era5 global reanalysis. *Quarterly Journal of the Royal Meteorological Society*, *146*(730), 1999–2049. doi: https://doi.org/10.1002/qj.3803

Hibbins, R. E., Espy, P. J., Orsolini, Y. J., Limpasuvan, V., & Barnes, R. J. (2019). Superdarn observations of semidiurnal tidal variability in the mlt and the response to sudden stratospheric warming events. *Journal of Geophysical Research: Atmospheres*, *124*(9), 4862-4872. doi: https://doi.org/10.1029/2018JD030157

Hocking, W., Fuller, B., & Vandepeer, B. (2001). Real-time determination of meteor-related parameters utilizing modern digital technology. *Journal of Atmospheric and Solar-Terrestrial Physics*, *63*(2), 155-169. doi: https://doi.org/10.1016/S1364-6826(00)00138-3

Hollingsworth, A. (1971). The effect of ocean and earth tides on the semi-diurnal lunar air tide. *Journal of Atmospheric Sciences*, *28*(6), 1021 - 1044. doi: https://doi.org/10.1175/1520-0469(1971)028⟨1021:TEOOAE⟩2.0.CO;2

Jacobi, C., Fröhlich, K., Viehweg, C., Stober, G., & Kürschner, D. (2007). Midlatitude mesosphere/lower thermosphere meridional winds and temperatures measured with meteor radar. *Advances in Space Research*, *39*(8), 1278-1283. doi: 10.1016/j.asr.2007.01.003

Jin, H., Miyoshi, Y., Pancheva, D., Mukhtarov, P., Fujiwara, H., & Shinagawa, H. (2012). Response of migrating tides to the stratospheric sudden warming in 2009 and their effects on the ionosphere studied by a whole atmosphere-ionosphere model gaia with cosmic and timed/saber observations. *Journal of Geophysical Research: Space Physics*, *117*(A10). doi: https://doi.org/10.1029/2012JA017650

Koushik, N., Kumar, K. K., Vineeth, C., Ramkumar, G., & Subrahmanyam, K. V. (2020). Meteor radar observations of lunar semidiurnal oscillations in the mesosphere lower thermosphere over low and equatorial latitudes and their variability during sudden stratospheric warming events. *Journal of Geophysical Research: Space Physics*, *125*(9), e2019JA027736. doi: https://doi.org/10.1029/2019JA027736

Limpasuvan, V., Orsolini, Y. J., Chandran, A., Garcia, R. R., & Smith, A. K. (2016). On the composite response of the mlt to major sudden stratospheric warming events with elevated stratopause. *Journal of Geophysical Research: Atmospheres*, *121*(9), 4518-4537. doi: https://doi.org/10.1002/2015JD024401

Lin, J. T., Lin, C. H., Lin, C. Y., Pedatella, N. M., Rajesh, P. K., Matsuo, T., & Liu, J. Y. (2019). Revisiting the modulations of ionospheric solar and lunar migrating tides during the 2009 stratospheric sudden warming by using global ionosphere specification. *Space Weather*, *17*(5), 767-777. doi: https://doi.org/10.1029/2019SW002184

Liu, G., Lieberman, R. S., Harvey, V. L., Pedatella, N. M., Oberheide, J., Hibbins, R. E., ... Janches, D. (2021). Tidal variations in the mesosphere and lower thermosphere before, during, and after the 2009 sudden stratospheric warming. *Journal of Geophysical Research: Space Physics*, *126*(3), e2020JA028827. doi: https://doi.org/10.1029/2020JA028827

Liu, H.-L., Bardeen, C. G., Foster, B. T., Lauritzen, P., Liu, J., Lu, G., ... Wang, W. (2018). Development and validation of the whole atmosphere community climate model with thermosphere and ionosphere extension (WACCM-x 2.0). *Journal of Advances in Modeling Earth Systems*, *10*(2), 381–402. doi: https://doi.org/10.1002/2017ms001232

Liu, H.-L., Wang, W., Richmond, A. D., & Roble, R. G. (2010). Ionospheric variability due to planetary waves and tides for solar minimum conditions. *Journal of Geophysical Research: Space Physics*, *115*(A6). doi: https://doi.org/10.1029/2009JA015188

Liu, J., Zhang, D., Goncharenko, L. P., Zhang, S.-R., He, M., Hao, Y., & Xiao, Z. (2021). The latitudinal variation and hemispheric asymmetry of the ionospheric lunitidal signatures in the american sector during major sudden stratospheric warming events. *Journal of Geophysical Research: Space Physics*, *126*(5), e2020JA028859. doi: https://doi.org/10.1029/2020JA028859

Lyard, F. H., Allain, D. J., Cancet, M., Carrère, L., & Picot, N. (2021). Fes2014 global ocean tide atlas: design and performance. *Ocean Science*, *17*(3), 615–649. doi: 10.5194/os-17-615-2021

McCormack, J. P., Hoppel, K., Kuhl, D., de Wit, R., Stober, G., Espy, P., ... Hibbins, R. (2017). Comparison of mesospheric winds from a high-altitude meteorological analysis system and meteor radar observations during the boreal winters of 2009–2010 and 2012–2013. *Journal of Atmospheric and Solar-Terrestrial Physics*, *154*, 132–166. doi: https://doi.org/10.1016/j.jastp.2016.12.007

Nath, D., Chen, W., Zelin, C., Pogoreltsev, A. I., & Wei, K. (2016). Dynamics of 2013 sudden stratospheric warming event and its impact on cold weather over eurasia: Role of planetary wave reflection. *Scientific Reports*, *6*(1). doi: 10.1038/srep24174

Pedatella, N. M., & Forbes, J. M. (2010). Evidence for stratosphere sudden warming-ionosphere coupling due to vertically propagating tides. *Geophysical Research Letters*, *37*(11). doi: https://doi.org/10.1029/2010GL043560

Pedatella, N. M., & Liu, H. (2013). The influence of atmospheric tide and planetary wave variability during sudden stratosphere warmings on the low latitude ionosphere. *Journal of Geophysical Research: Space Physics*, *118*(8), 5333-5347. doi: 10.1002/jgra.50492

Pedatella, N. M., Liu, H.-L., & Richmond, A. D. (2012). Atmospheric semidiurnal lunar tide climatology simulated by the whole atmosphere community climate model. *Journal of Geophysical Research: Space Physics*, *117*(A6). doi: https://doi.org/10.1029/2012JA017792

Pedatella, N. M., Liu, H.-L., Sassi, F., Lei, J., Chau, J., & Zhang, X. (2014). Ionosphere variability during the 2009 ssw: Influence of the lunar semidiurnal tide and mechanisms producing electron density variability. *Journal of Geophysical Research: Space Physics*, *119*(5), 3828-3843. doi: https://doi.org/10.1002/2014JA019849

Picone, J. M., Hedin, A. E., Drob, D. P., & Aikin, A. C. (2002). NRLMSISE-00 empirical model of the atmosphere: Statistical comparisons and scientific issues. *Journal of Geophysical Research: Space Physics*, *107*(A12), SIA 15–1–SIA 15–16. doi: https://doi.org/10.1029/2002ja009430

Stober, G., Baumgarten, K., McCormack, J. P., Brown, P., & Czarnecki, J. (2020). Comparative study between ground-based observations and navgem-ha analysis data in the mesosphere and lower thermosphere region. *Atmospheric Chemistry and Physics*, *20*(20), 11979–12010. doi: 10.5194/acp-20-11979-2020

Stober, G., Kuchar, A., Pokhotelov, D., Liu, H., Liu, H.-L., Schmidt, H., … Mitchell, N. (2021). Interhemispheric differences of mesosphere–lower thermosphere winds and tides investigated from three whole-atmosphere models and meteor radar observations. *Atmospheric Chemistry and Physics*, *21*(18), 13855–13902. doi: 10.5194/acp-21-13855-2021

Stober, G., Liu, A., Kozlovsky, A., Qiao, Z., Kuchar, A., Jacobi, C., … Mitchell, N. (2022). Meteor radar vertical wind observation biases and mathematical debiasing strategies including the 3dvar+div algorithm. *Atmospheric Measurement Techniques*, *15*(19), 5769–5792. doi: 10.5194/amt-15-5769-2022

Swinbank, R., & Ortland, D. A. (2003). Compilation of wind data for the upper atmosphere research satellite (uars) reference atmosphere project. *Journal of Geophysical Research: Atmospheres*, *108*(D19). doi: https://doi.org/10.1029/2002JD003135

Teitelbaum, H., & Vial, F. (1991). On tidal variability induced by nonlinear interaction with planetary waves. *Journal of Geophysical Research: Space Physics*, *96*(A8), 14169-14178. doi: https://doi.org/10.1029/91JA01019

van Caspel, W. E., Espy, P. J., Ortland, D. A., & Hibbins, R. E. (2022). The mid- to high-latitude migrating semidiurnal tide: Results from a mechanistic tide model and superdarn observations. *Journal of Geophysical Research: Atmospheres*, *127*(1), e2021JD036007. doi: https://doi.org/10.1029/2021JD036007

Vial, F., & Forbes, J. (1994, oct). Monthly simulations of the lunar semi-diurnal tide. *Journal of Atmospheric and Terrestrial Physics*, *56*(12), 1591–1607. doi: https://doi.org/10.1016/0021-9169(94)90089-2

Wu, Q., Ward, W., Kristoffersen, S., Maute, A., & Liu, J. (2019). Simulation and observation of lunar tide effect on high-latitude, mesospheric and lower thermospheric winds during the 2013 sudden stratospheric warming event. *Journal of Geophysical Research: Space Physics*, *124*(2), 1283-1291. doi: https://doi.org/10.1029/2018JA025476

Xiong, J., Wan, W., Ding, F., Liu, L., Ning, B., & Niu, X. (2013). Coupling between mesosphere and ionosphere over beijing through semidiurnal tides during the 2009 sudden stratospheric warming. *Journal of Geophysical Research: Space Physics*, *118*(5), 2511-2521. doi: https://doi.org/10.1002/jgra.50280

Zhang, J., Limpasuvan, V., Orsolini, Y. J., Espy, P. J., & Hibbins, R. E. (2021). Climatological westward-propagating semidiurnal tides and their composite response to sudden stratospheric warmings in superdarn and sd-waccm-x. *Journal of Geophysical Research: Atmospheres*, *126*(3), e2020JD032895. doi: https://doi.org/10.1029/2020JD032895

Zhang, X., & Forbes, J. M. (2014a). Lunar tide in the thermosphere and weakening of the northern polar vortex. *Geophysical Research Letters*, *41*(23), 8201-8207. doi: 10.1002/2014GL062103

Zhang, X., & Forbes, J. M. (2014b). Lunar tide in the thermosphere and weakening of the northern polar vortex. *Geophysical Research Letters*, *41*(23), 8201-8207. doi: https://doi.org/10.1002/2014GL062103

A case study of the solar and lunar semidiurnal tide response to the 2013 sudden stratospheric warming

Willem E. van Caspel[1,2,*], Patrick Espy[1,2], Robert Hibbins[1,2], Gunter Stober[3], Peter Brown[4], Christoph Jacobi[5], Johan Kero[6]

[1]Department of Physics, Norwegian University of Science and Technology (NTNU), Trondheim, Norway
[2]Birkeland Centre for Space Science, Bergen, Norway
[3]Institute of Applied Physics and Oeschger Center for Climate Change Research, Microwave Physics, University of Bern, Bern, Switzerland
[4]Department of Physics and Astronomy, Western University, London, Ontario, Canada
[5]Leipzig University, Leipzig, Germany
[6]Swedish Institute of Space Physics, Kiruna, Sweden

Key Points:

- Simulations of the SDT are compared against meteor wind observations in the mid-to-high latitude northern hemisphere during the 2013 SSW
- Individual lunar and solar SDT simulations find that the net tidal response is largely driven by the solar component
- The response of the solar SDT is driven by changing zonal mean propagation conditions and by non-linear interactions with planetary waves

* Now at Research and Development Department, Norwegian Meteorological Institute, Oslo, Norway

Corresponding author: Willem van Caspel, `willemvc@met.no`

Abstract

This study investigates the response of the semidiurnal tide (SDT) to the 2013 major sudden stratospheric warming (SSW) event using meteor radar wind observations and mechanistic tidal model simulations. In the model, the background atmosphere is constrained to meteorological fields from the Navy Global Environmental Model - High Altitude analysis system. The solar (thermal) and lunar (gravitational) SDT components are forced by incorporating hourly temperature tendency fields from the ERA5 forecast model, and by specifying the M_2 and N_2 lunar gravitational potentials, respectively. The simulated SDT response is compared against meteor wind observations from the CMOR (43.3°N, 80.8°W), Collm (51.3°N, 13.0°E), and Kiruna (67.5°N, 20.1°E) radars, showing close agreement with the observed amplitude and phase variability. Numerical experiments investigate the individual roles of the solar and lunar SDT components in shaping the net SDT response. Further experiments isolate the impact of changing propagation conditions through the zonal mean background atmosphere, non-linear wave-wave interactions, and the SSW-induced stratospheric ozone redistribution. Results indicate that between 80-97 km altitude in the northern hemisphere mid-to-high latitudes the net SDT response is driven by the solar SDT component, which itself is shaped by changing propagation conditions through the zonal mean background atmosphere and by non-linear wave-wave interactions. In addition, it is demonstrated that as a result of the rapidly varying solar SDT during the SSW the contribution of the lunar SDT to the total measured tidal field can be significantly overestimated.

1 Introduction

During wintertime, planetary waves can propagate upwards from the troposphere into the stratosphere (Charney & Drazin, 1961). There they can destabilize the westerly winds of the stratospheric polar vortex, potentially leading to a vortex split or displacement event. The planetary wave breaking associated with such events induces enhanced stratospheric poleward meridional flows, leading to rapid compressional heating, or sudden stratospheric warming (SSW). Moreover, the westward momentum forcing exerted by the planetary waves causes a reversal of the otherwise westerly winds. While most of the dynamical changes associated with SSWs occur in the mid- and high-latitude stratosphere, their impact can extend from the troposphere up into the thermosphere (Limpasuvan et al., 2016). In the mid- and high-latitude mesosphere-lower-thermosphere (MLT, 80-110 km altitude), one of the major sources of SSW variability is associated with the induced changes to the semidiurnal tide (SDT) (Baldwin et al., 2021).

The SDT is an atmospheric inertio-gravity wave that is expressed as a near 12-hour oscillation in the atmospheric winds, temperature and pressure fields (Chapman & Lindzen, 1970). While it is predominantly excited by radiative and latent heating in the lower atmosphere following the daily insulation cycle, the SDT reaches its largest amplitudes in the MLT due to the decreasing density of the atmosphere with altitude (Hagan, 1996). An additional excitation mechanism for the SDT arises from the lunar gravitational potential, which excites waves with near integer fractions of a lunar day periods. Through neutral atmosphere and ionosphere coupling, the different SDT components are also observed in ionospheric parameters such as equatorial E $\times$ B plasma drift velocities, F-region electron densities, ion temperatures, and sporadic E occurrence frequencies (Pedatella et al., 2014; Arras et al., 2009).

The SDT signature in the upper atmosphere is strongly influenced by the tidal propagation conditions through the underlying atmosphere (van Caspel et al., 2022). The SDT therefore represents an important coupling mechanism between the variability of the lower and middle atmosphere and that of the MLT and ionosphere system (Pedatella & Forbes, 2010; Forbes, 2009). This coupling is especially pronounced during SSWs, when tidal propagation conditions rapidly change (L. P. Goncharenko et al., 2021). However, open questions remain about the spatio-temporal drivers of the SDT response, in particular regarding the individual roles and driving mechanisms of the solar and lunar SDT components (L. P. Goncharenko et al., 2022; J. Liu et al., 2021; G. Liu et al., 2021; J. Zhang et al., 2021; Wu et al., 2019).

The SDT response is challenging to investigate due to the large number of physical mechanisms involved. These include changes to the propagation conditions of the individual solar (12.00 hr) and lunar M_2 (12.42 hr) and N_2 (12.64 hr) components (Forbes & Zhang, 2012; Jin et al., 2012), non-linear wave-wave interactions with quasi-stationary planetary waves (H.-L. Liu et al., 2010), and changes to the thermal forcing caused by a redistribution of stratospheric ozone (L. P. Goncharenko et al., 2012). Quantifying the individual contributions of these mechanisms to the net SDT response is further complicated by the need for time windows upwards of 15 days to separate the lunar and solar components from a single time series (J. Liu et al., 2021; Lin et al., 2019; X. Zhang & Forbes, 2014a). Such long time windows can easily lead to an overly smoothed and potentially cross-contaminated view of the SDT response, especially considering that SSW-induced SDT variability can occur over the course of a few days (Stober et al., 2020).

In this study, SDT observations from a range of Northern Hemisphere mid- and high-latitude meteor wind radars are simulated using a mechanistic tidal model during the 2013 major SSW event. The model, called the PRimitive equations In Spherical harmonics Model (PRISM), is a high-top neutral atmosphere model that allows for a free specification of the background atmosphere and tidal forcing terms (van Caspel et al., 2022). The background atmosphere is specified to realistic three-dimensional winds and temperatures, and the SDT is forced by incorporating a detailed thermal and gravitational forcing scheme. The gravitational scheme includes both the M_2 and N_2 lunar SDT components, and incorporates ocean and load tide elevation fields from a global ocean tidal model.

Section 2 describes the implementation of the solar and lunar tidal forcing terms, and of the background atmospheric specification. In Section 3, the simulated SDT response is compared to measurements from the CMOR (43.3°N, 80.8°W), Collm (51.3°N, 13.0°E), and Kiruna (67.5°N, 20.1°E) meteor wind radars between 80-97 km altitude. In addition, individual simulations of the lunar and solar SDT components are performed to establish the relative importance of these tidal components in shaping the net simulated SDT response. In Section 4, numerical experiments are performed to assess the impact of the changing propagation conditions through the zonal mean background atmosphere, non-linear wave-wave interactions with quasi-stationary planetary waves, and of changes to the thermal forcing resulting from a redistribution of stratospheric ozone. The results are discussed and concluded in Section 5.

2 Model Description

PRISM is a non-linear and time-dependent spectral model, which in earlier work has been used to simulate the SDT in the mid-latitude MLT (van Caspel et al., 2022). The model includes a climatological description of tidal dissipation terms through ion drag, Newtonian cooling, eddy diffusion, molecular diffusion, and surface friction. In this study, the horizontal resolution is truncated at zonal wavenumber S = 9 and meridional wavenumber N = 24, with 161 vertical levels up to an altitude of ∼430 km. While a detailed description of the model can be found in van Caspel et al. (2022) and references therein, those aspects of the model which have been modified for the current work are discussed below.

2.1 Background Atmosphere

The three-dimensional background atmosphere can be freely specified by relaxing the model's dynamical fields towards that of the input meteorology, for which a nudging rate of $D = 1/3$ days^{-1} (d^{-1}) is used. This nudging rate is high enough to accurately represent the spatial and temporal evolution of the polar vortex, while being low enough to have no effect on the simulated SDT wave-field. To minimize the effect of wave-mean flow interactions between the zonal mean background atmosphere and the artificially introduced planetary waves (Pedatella & Liu, 2013), the zonal mean spherical harmonic coefficients are nudged at a rate of $D_0 = 4$ d^{-1}. While this may damp non-migrating zonal mean SDT components, diagnostic simulations with a lower zonal mean nudging rate find that this tidal component does not contribute significantly to our results.

The background atmosphere between 85-0.001 hPa (approximately 10-95 km altitude) is nudged to daily mean wind and temperature fields calculated from 3-hourly NAVGEM-HA meteorological analysis data. The NAVGEM-HA model incorporates satellite observations of ozone, water vapor, and temperatures in the stratosphere and mesosphere, as well as standard operational meteorological observations in the troposphere (McCormack et al., 2017). Previous studies have shown that the NAVGEM-HA mean winds and temperatures are in good agreement with observations during the 2013 SSW event (Stober et al., 2020; McCormack et al., 2017).

Fig. 1a illustrates the temporal evolution of the 2013 SSW in both the daily mean NAVGEM-HA fields and in PRISM, using the definition of Polar Vortex Weakening (PVW) proposed by X. Zhang and Forbes (2014b). According to this definition, the day of peak PVW occurs on January 10th 2013. On this day, zonal mean zonal winds at 48 km altitude and 70°N reach their most easterly phase, coincident with zonal mean temperatures at 40 km altitude and 90°N reaching a maximum. Within the context of this work, the SSW onset is taken as the point where the zonal mean zonal winds at 48 km altitude and 70°N reverse, on January 3rd. The onset of the recovery phase is taken as the point where the zonal mean zonal winds return to their climatological westerlies, on January 22nd. However, throughout the following text, the onset date, day of peak PVW, and recovery phase are referred to by their number of days since the 1st of December 2012 (day 34, 41, and 53, respectively), which is the starting date of the simulations.

To demonstrate the accurate representation of the polar vortex in PRISM, Fig. 1b shows the evolution of quasi-stationary planetary waves with zonal wavenumber 1 (PW1) and 2 (PW2) in the NAVGEM-HA and PRISM zonal winds at 48 km altitude. The wave amplitudes are calculated by least-squares fitting stationary PW1 and PW2 waves to 4-day running mean zonal wind data, averaged between 50-70°N. The planetary wave structure in PRISM closely follows that of NAVGEM-HA, which is marked by a PW1 enhancement leading up to the end of December, followed by a PW2 amplification in early January. This temporal evolution of the planetary wave structure is also consistent with earlier studies of the 2013 SSW event (Nath et al., 2016; Coy & Pawson, 2015; L. Goncharenko et al., 2013).

Below an altitude of 85 hPa, PRISM is nudged to daily mean winds and temperatures calculated from 1-hourly ECMWF ERA5 reanalysis data (Hersbach et al., 2020). Above 0.001 hPa, the model is nudged to daily mean wind and temperature fields calculated from the Horizontal Wind Model version 2014 (HWM14, Drob et al., 2015) and from the NRLMSISE-00 reference model (Picone et al., 2002), respectively. Diagnostic simulations where the boundaries between the different datasets of the composite atmosphere are artificially smoothed, find that any discontinuities between the datasets do not significantly effect the simulated SDT field.

2.2 Solar Forcing

The solar thermal SDT is forced by incorporating hourly global temperature tendency fields (TTFs) from the ECMWF Integrated Forecasting System (IFS) cycle 41r2 forecast model (Ehard et al., 2018). These TTFs include radiative and latent heating effects from the surface up to ~80 km altitude, and are interpolated onto the PRISM model time-step. The ERA5 forecast model is initialized twice daily at 06:00 and 18:00 UTC based on a broad range of observations, and the 12 hr segments following each initialization are used

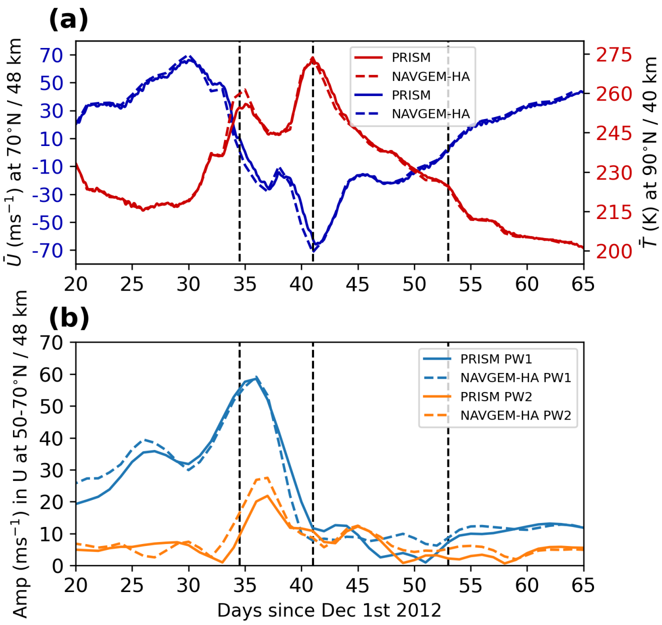

Figure 1. Panel **(a)** shows the time development of PVW as simulated by PRISM (solid lines) and by the NAVGEM-HA model (dotted lines). Panel **(b)** shows the corresponding time development of the PW1 and PW2 amplitudes in the zonal wind at 48 km altitude averaged between 50-70°N. The vertical dashed lines mark the SSW onset, peak PVW, and recovery dates as defined in Section 2.1.

to construct a continuous dataset of hourly TTFs. While the IFS TTFs extend only up to an altitude of ~80 km, the contribution to the simulated SDT by the tide forced above this altitude is very small compared to those forced in the tropospheric and stratospheric regions (van Caspel et al., 2022).

One limitation of the IFS TTFs is that its radiative transfer model does not include interactive ozone chemistry, but instead specifies a climatological zonal mean stratospheric ozone distribution (ECMWF, 2020). Consequently, the IFS TTFs cannot describe the thermal forcing changes caused by a redistribution of stratospheric ozone. In Section 4.2.1, this limitation is addressed by using 3-hourly TTFs from the Specified Dynamics Whole Atmosphere Community Climate Model with Thermosphere Extension version 2.1 (SD-WACCMX, H.-L. Liu et al., 2018). However, while the SD-WACCMX TTFs include interactive ozone chemistry, diagnostic simulations find that the short-term variability of the solar SDT forcing is better represented in the IFS forecast model.

2.3 Lunar Forcing

Following the approach of Pedatella et al. (2012), the lunar M_2 (12.42 hr) and N_2 (12.66 hr) SDT components are prescribed by including the momentum forcing arising from the horizontal gradient of the lunar tidal potentials. The tidal potential is described by its contributions arising from the lunar gravitational potentials (Ω), the vertical displacement of the ocean, load, and solid Earth tides ($g\zeta$, where $g = 9.81$ ms^{-1} and ζ is the vertical displacement in meters), and the tidally induced redistribution of solid Earth mass (Ω^e). The potential arising from the tidally induced redistribution of ocean mass represents only a very minor contribution (Vial & Forbes, 1994), and is ignored in this work.

The lunar gravitational potentials are described by

$$\begin{aligned}\Omega_{M_2} &= -0.7933P_2^2(\theta)\cos(2\tau)\\ \Omega_{N_2} &= -0.1518P_2^2(\theta)\cos(2\tau - s + p)\end{aligned}$$

in units of m^2s^{-2}, where $P_2^2(\theta) = 3\sin^2\theta$ is an associated Legendre polynomial and θ is co-latitude (Chapman & Lindzen, 1970). In the above time factors, $\tau = t + h - s$ where h, s, and p are given by

$$\begin{aligned}h &= 279.69668 + 36000.76892T + 0.00030T^2\\ s &= -270.43659 + 481267.89057T + 0.00198T^2\\ p &= 334.32956 + 4069.03403T - 0.01032T^2 - 0.00001T^3\end{aligned}$$

in units of degrees. Here T represents the time since Greenwich mean noon on 1899 December 31 (epoch 1900) in units of a Julian century (36525 days), and t is the angular measure of mean solar time ($15^\circ = 1$ hr). The M_2 potential describes the classic double tidal bulge, while the N_2 potential describes the $\sim 20\%$ amplitude variations of the M_2 potential caused by the ellipticity of the lunar orbit.

The Earth tide accounts for the vertical displacement of the Earth's crust in response to the lunar gravitational field. Furthermore, the Earth tide is accompanied by a geopotential perturbation arising from the associated redistribution of crustal mass. Both the Earth tide and the associated mass-redistribution potentials can be expressed as Love-number multiplications of the lunar gravitational potentials, where the Love numbers are given by $h_2 = -0.609$ and $k_2 = 0.302$, respectively (Hollingsworth, 1971). The M_2 and N_2 Earth tide potential can then be written as $(\zeta^e_{M_2} + \zeta^e_{N_2})g = h_2(\Omega_{M_2} + \Omega_{N_2})$, and the associated mass-redistribution potential as $\Omega^e_{M_2} + \Omega^e_{N_2} = k_2(\Omega_{M_2} + \Omega_{N_2})$.

To force the lunar ocean and load tide components, hourly M_2 and N_2 elevation fields from the FES2014 ocean tide atlas are incorporated. The FES2014 model combines the hydrodynamic modeling of the ocean tides with ensemble data assimilation techniques, providing global instantaneous ocean and load tide elevation fields (Lyard et al., 2021). While the ocean tide represents the vertical displacement of the ocean surface, the load tide represents the vertical displacement of the ocean crust in response to the loading by the ocean tides.

To verify the implementation of the lunar tide forcing, migrating lunar SDT (lunar SW2, for Semidiurnal, Westward S = 2) simulations are compared against climatological simulations from the Global Scale Wave Model (GSWM) and Whole-Atmosphere Community Climate Model (WACCM), as described in detail in Pedatella et al. (2012). While the GSWM and WACCM simulations do not include the N_2 tidal potentials, these tidal components have very little impact on the monthly mean amplitudes discussed in the following. For the PRISM lunar validation simulation, the lunar tide forcing for the year 2013 is propagated through a climatological background atmosphere based on monthly mean zonal mean zonal winds and temperatures from the upper atmosphere research satellite (UARS) reference atmosphere project (URAP, Swinbank & Ortland, 2003). The URAP atmosphere extends from the surface up to ~110 km altitude, and is padded to HWM14 and MSISE-00 fields for altitudes above that. No thermal forcing is included in the lunar validation simulation, such that the amplitude of the lunar SW2 can easily be extracted using 4-day sliding window Fourier analysis.

Fig. 2 shows the simulated mean January and June lunar SW2 amplitudes in the zonal winds. The vertical and latitudinal tidal structure follows those simulated by the GSWM and WACCM models, as shown in Pedatella et al. (2012), with peak amplitudes occurring in the summer hemisphere between 40-50° latitude and 110-125 km altitude. Amplitudes in the winter hemisphere are around a factor of two smaller, and maximize roughly between 100-120 km. We note that, while Pedatella et al. (2012) find that GSWM lunar amplitudes

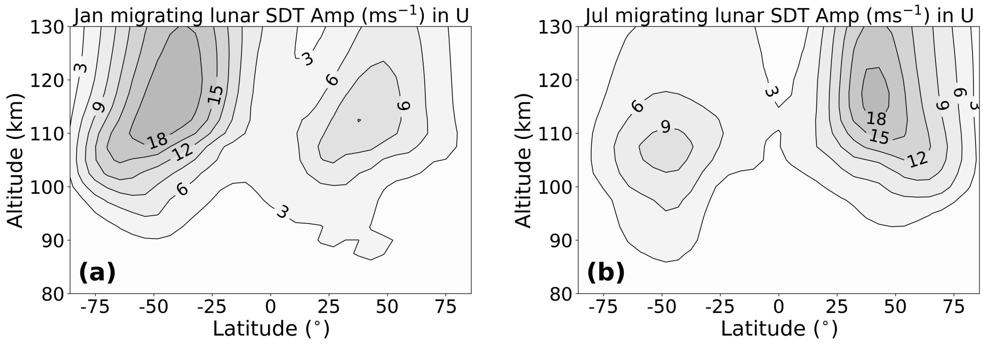

Figure 2. Monthly mean lunar SW2 amplitude in the zonal winds simulated by the climatological PRISM lunar tide simulation for January **(a)** and July **(b)**.

are a factor of 2-3 greater than those simulated by WACCM, the magnitude of the amplitudes simulated by PRISM more closely agree with those of the GSWM. For example, peak amplitudes in January are around 18 ms^{-1} in PRISM, 8 ms^{-1} in WACCM, and 22 ms^{-1} in GSWM.

3 Comparison to Observations

In this section, the simulated SDT response is compared against meteor wind observations from the CMOR, Collm, and Kiruna meteor radar sites. The relative importance of the solar and lunar SDT components is quantified by comparison against individual lunar and solar SDT simulations. We note that the results presented in this section do not depend on the choice of zonal or meridional winds, and therefore only the zonal component is discussed.

3.1 SDT Response

The CMOR, Collm, and Kiruna meteor radars provide hourly horizontal winds by measuring the so-called meteor trail position data (Hocking et al., 2001), with details of the radars and wind retrieval algorithm given by Stober et al. (2022, 2021). We note that the Collm meteor radar received an upgrade in 2015, with the 2012/2013 configuration described in more detail by Jacobi et al. (2007). In the current work, meteor radar wind measurements between 80-97 km altitude are used, having vertical resolutions between 2-3 km. To extract the SDT amplitude and phase from the hourly winds, a least-squares 4-day sliding window fit of a mean and sine waves representing the diurnal, semidiurnal and terdiurnal tides is performed. Here the fitted SDT includes only a 12.00 hr wave, since the employed 4-day time window effectively aliases the solar and lunar SDT components. To compare the model to observation, hourly PRISM output is interpolated to the geographic locations of the meteor radars, and analyzed using the same least-squares fitting routine.

Fig. 3 shows the measured and simulated amplitude of the SDT at the three radar sites. At the CMOR site (Fig. 3a and 3d), both the model and observations show a pronounced amplitude enhancement occurring roughly five days after peak PVW, with amplitudes reaching up to 70 ms^{-1}. This enhancement is preceded by a 10-day amplitude minimum of around 10-20 ms^{-1}, starting around the time of the SSW onset. Notably, a quasi 10-day periodicity is discernible in both the observed and simulated amplitudes, reaching local amplitude maxima around days 24, 31, 46, and 60. This periodicity is also observable at the CMOR and Kiruna sites, and will be discussed in more detail in Section 4.

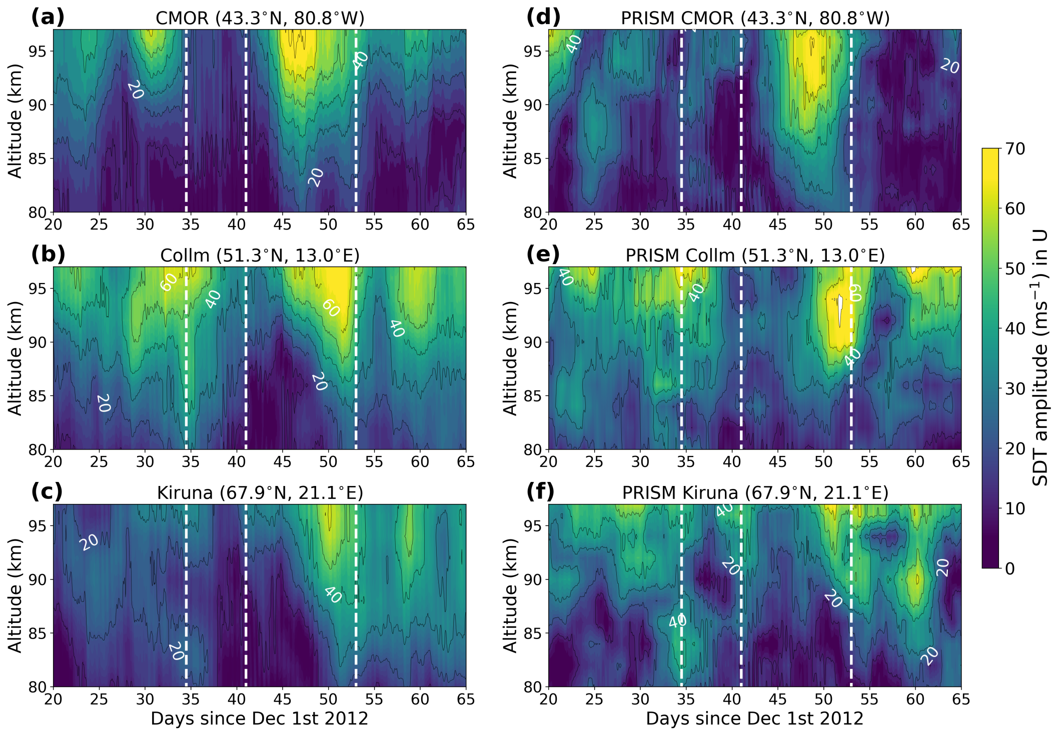

Figure 3. Comparison of the zonal SDT amplitude measured and simulated at the CMOR **(a,d)**, Collm **(b,e)**, and Kiruna **(c,f)** radar sites. Contours are spaced in 10 ms^{-1} intervals. The vertical dashed lines mark the SSW onset, peak PVW, and recovery onset as defined in Section 2.1.

At the Collm site (Fig. 3b and 3e), the observed and simulated SDT also show an amplitude enhancement with 60-70 ms^{-1} maximum, although here peak amplitudes occur nearer to 10 days after peak PVW. Similar to the CMOR site, the SDT enhancement is preceded by a ~10-day amplitude minimum. At the Kiruna site (Fig. 3c and 3f), the simulated and observed SDT is similar to the other sites, reaching peak amplitudes in the range of 50-60 ms^{-1} around 10 days after peak PVW. Here the preceding amplitude minimum is less pronounced, however, as amplitudes leading up to the onset date are comparatively smaller. The model also shows more variability in the vertical compared to observation, while amplitudes are overestimated by around 20 ms $^{-1}$ between days 20 and 40.

Fig. 4 shows the phase of the simulated and observed SDT at the three radar sites, expressed here in terms of the Local Time Of Maximum (LTOM). The local time at each radar site is calculated as $t_{local} = t_{UTC} + 24 \cdot \lambda/360$, where λ is the station longitude in degrees. The observed phase displays similar characteristics at all three radar sites, where the LTOM shifts to an earlier time by about 3-4 hr over the course of a five day period following peak PVW. While this behavior is reproduced by the model at all three sites, the simulated phase shift is instead nearer to 2-3 hr. In addition, the simulated phase at the Kiruna site is overestimated by about 2 hrs on average, while the phase at the CMOR site displays more variability than observation between days 50 and 65.

3.2 Solar and Lunar SDT Response

Numerical experiments are performed to investigate the individual contributions of the lunar and solar SDT components to the total simulated SDT. This is achieved by performing simulations where only the lunar SDT forcing (OnlyLunar) or only the thermal forcing

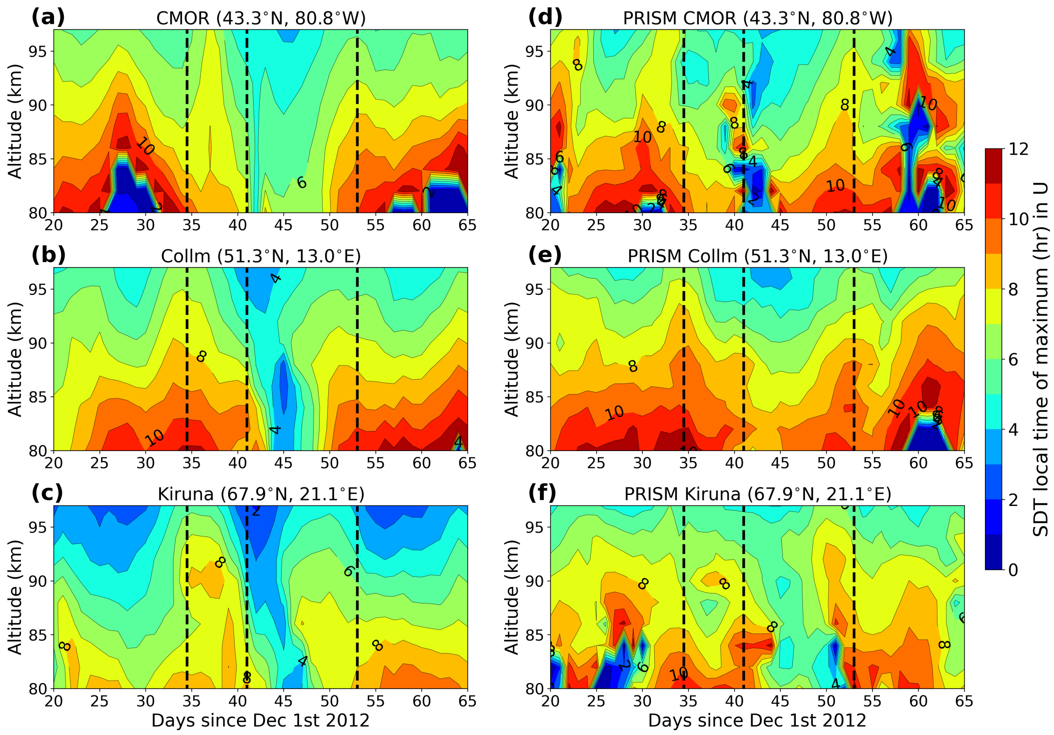

Figure 4. Comparison of the zonal SDT phase (LTOM) simulated by PRISM and measured by the CMOR **(a,d)**, Collm **(b,e)**, and Kiruna **(c,f)** meteor radars. Contours are spaced in 1 hr intervals. The vertical dashed lines mark the SSW onset, peak PVW, and recovery onset as defined in Section 2.1.

(OnlySolar) are included. Fig. 5 compares the two simulations, where the solar SDT is denoted by S_2 and the lunar SDT by M_2. As before, the tidal amplitudes are calculated using a 4-day sliding window, but now the least-squares fit to the OnlyLunar simulation uses a 12.42 hr wave rather than a 12.00 hr wave (although the results are very similar using either a 12.00 hr or 12.42 hr wave period). Fig. 5a-c shows that the simulated solar SDT closely resembles that of the full PRISM simulation (shown in Fig. 3d-f). The most notable differences with the full PRISM simulation are that the amplitude enhancements following peak PVW are 5-10 ms^{-1} lower, while the amplitude minima preceding the enhancements are 5-10 ms^{-1} higher.

Fig. 5d-f shows that the lunar SDT enhances broadly between peak PVW and the recovery phase onset, reaching amplitudes between 12-14 ms^{-1} at all three radar sites. The magnitude of the lunar SDT amplitude is only around 15-20% of that of the solar SDT at the time of the enhancement. Furthermore, a diagnostic simulation without the lunar N_2 forcing included shows difference of less than 3 ms^{-1} with the OnlyLunar simulation, indicating that there is no particular enhancement of the N_2 component taking place. In agreement with lunar amplitudes being considerably smaller than the solar component, diagnostic analysis finds that the phase behavior of the SDT over the course of the SSW closely follows that of the solar component.

It is important to note that the OnlySolar and OnlyLunar simulations cannot capture the effects of any wave-wave interactions between the solar and lunar SDT components. However, diagnostic analysis finds that the sum of the OnlySolar and OnlyLunar simulations closely matches that of the PRISM simulation, suggesting that tidal wave-wave interactions

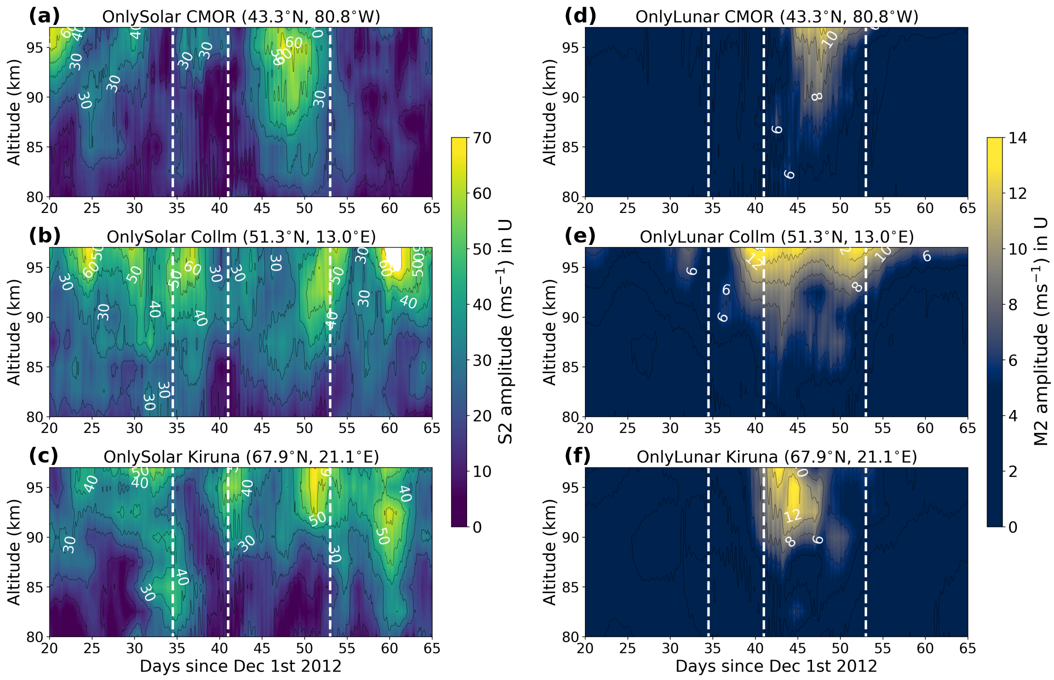

Figure 5. Comparison of the zonal SDT amplitude simulated by the OnlySolar and OnlyLunar simulations at the CMOR **(a,d)**, Collm **(b,e)**, and Kiruna **(c,f)** sites. Contours are spaced in 10 ms^{-1} intervals for the left-hand panels, and 4 ms^{-1} intervals for the right-hand panels. The vertical dashed lines mark the SSW onset, peak PVW, and recovery onset as defined in Section 2.1.

are limited. We note that differences between the sum of the OnlySolar and OnlyLunar simulations and the full PRISM simulation can also arise from a certain degree of internal variability, or noise, present from simulation to simulation. This noise can lead to SDT amplitude variations on the order of a few ms^{-1}, which we attribute to internal gravity wave variability.

4 Model Analysis

Further numerical experiments are performed to quantify the individual contributions to the simulated SDT response of the changing propagation conditions through the zonal mean background atmosphere, non-linear wave-wave interactions with quasi-stationary planetary waves, and thermal forcing variations caused by a stratospheric ozone redistribution. An overview of the experiments of this section is given in Table 1.

4.1 Migrating and Non-Migrating SDT Response

To gain insight into the drivers of the SDT response, the simulated tidal wave field is decomposed into its migrating and non-migrating components. These tidal components are calculated by performing a 4-day sliding window 2-D Fourier decomposition of the simulated zonal wind field. In the simulation results, the two gravest non-migrating components are found to be the westward zonal wavenumber S = 1 (SW1) and westward zonal wavenumber S = 3 (SW3) tides (consistent with the results of Stober et al. (2020)), which can be produced by the interaction between the migrating SDT (SW2) and quasi-stationary PW1 waves (Angelats i Coll & Forbes, 2002; Teitelbaum & Vial, 1991). Non-migrating tides other than these two components are not discussed here.

Table 1. Numerical experiment model setup.

Experiment	Configuration
PRISM	Model configuration as described in Section 2
OnlyLunar	As PRISM, only lunar SDT forcing
OnlySolar	As PRISM, only solar SDT forcing
FixedAtmos	As OnlySolar, atmosphere fixed to zonal mean Dec 20th 2012
FixedForcing	As OnlySolar, forcing includes only SW2 fixed to Dec 20th 2012
FixedForcingZM	As FixedForcing, no background planetary waves included
WACStrat	As OnlySolar, forcing only between 100-0.1 hPa based on SD-WACCMX

Fig. 6a-c shows the latitude-time development of the SW1, SW2, and SW3 amplitudes in the PRISM simulation at 97 km altitude, corresponding to the highest altitude of the Collm, CMOR, and Kiruna meteor wind measurements. However, the results are independent of the choice of altitude for the altitude range considered in this work. The SW1 tide reaches amplitudes up to 27 ms^{-1} both before and after peak PVW, though amplitudes are generally highest for the period between peak PVW and the recovery onset. The largest SW1 tide amplitudes are, however, contained to latitudes above 50°N. Fig. 6b illustrates that the largest amplitudes occur in the SW2 component, consistent with the results of Hibbins et al. (2019). One notable feature of the SW2 tide is that its amplitudes are reduced by 20-30 ms^{-1} during a 10-day period centered roughly on the day of peak PVW. Furthermore, while the SW2 tide generally peaks between 50-70°N, its amplitude is increased between days 43-48 around 30-45°N, corresponding to the latitude band of the CMOR radar. SW2 amplitudes nevertheless stay below 45 ms^{-1} at all latitudes up until day 60. For the SW3 tide, amplitudes intermittently reach values between 10-20 ms^{-1} both before, after, and during the SSW.

In Fig. 6, the horizontal lines mark the latitudes of the meteor radars. Tracing, for example, the latitude of the Kiruna radar, shows that around the time of the peak amplitude enhancement (day 50, reaching up to 60 ms^{-1}), nearly half of the local amplitude is the result of the constructive interference between non-migrating tides and the SW2 tide. Similarly, over half of the peak amplitude of 70 ms^{-1} at the CMOR radar is the result of non-migrating tides, as SW2 amplitudes reach only up to around 30 ms^{-1} around that time.

In Fig. 6d-f the latitude-time development of the SW1, SW2, and SW3 tides in the OnlySolar simulation are shown. The close correspondence between these results and those of the PRISM simulation reaffirm the minimal role of the lunar SDT at these altitudes. Therefore, in the following investigation of the driving mechanisms of the SDT response, only the solar tidal components are considered.

4.2 Forcing Mechanisms

To isolate the impact of variations in the thermal forcing, the background atmosphere in the FixedAtmos experiment is fixed to that of the 20th December 2012, representing pre-SSW conditions. In addition, no planetary waves are included, such that any variations in the simulated non-migrating tides are caused by variations in the thermal forcing itself. Excluding the planetary waves is achieved by nudging the wave field towards zero rather than the daily mean NAVGEM-HA fields. Fig. 7a-c shows the resulting latitude-time development of the SW1, SW2, and SW3 tidal amplitudes. At the meteor radar latitudes, SW1 amplitudes remain mostly below 5 ms^{-1}, but reach up to 10 ms^{-1} around day 60. Fig. 7b shows that the resulting SW2 tide is marked by a quasi 10-day periodicity, having variations on the order of 10-20 ms^{-1}. This periodicity is also observed in the PRISM and OnlySolar

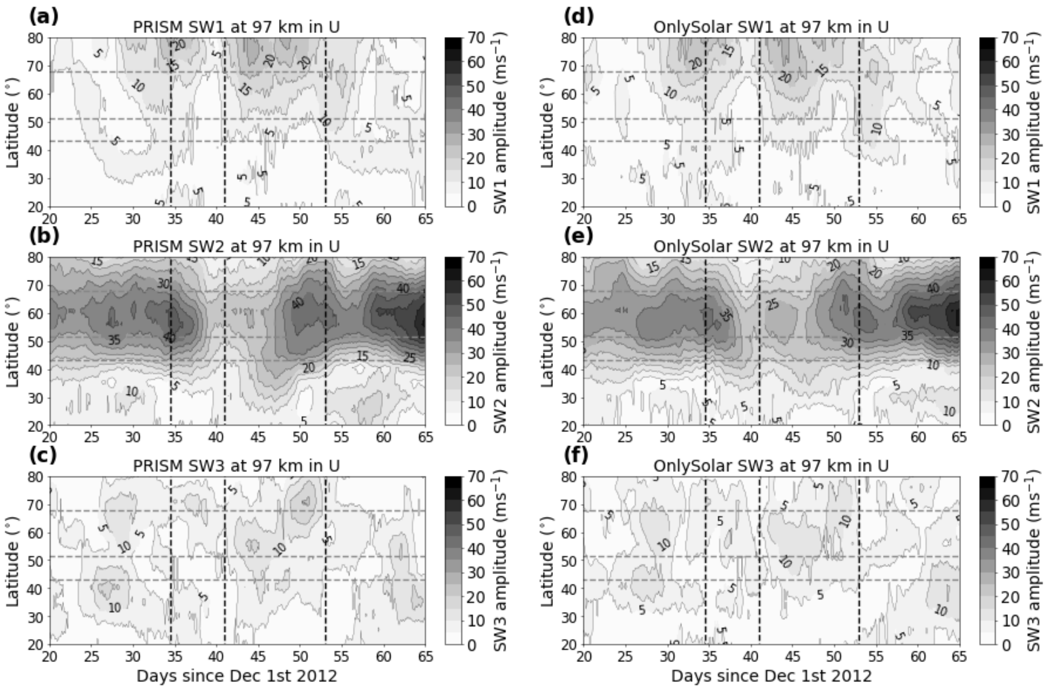

Figure 6. Latitude-time development of the zonal SW1, SW2, and SW3 amplitudes at 97 km altitude from the PRISM **(a,b,c)** and OnlySolar **(d,e,f)** simulations. The vertical dashed lines mark the SSW onset, peak PVW, and recovery onset as defined in Section 2.1. The horizontal dashed lines mark the latitudes of the three meteor radars used in this study.

simulations at the CMOR, Collm, and Kiruna meteor radar sites, as discussed in Section 3. Note that these variations are the results of variations in the tropospheric forcing, as the stratospheric forcing is based on a climatological ozone distribution. The SW3 tide shown in Fig. 7c reaches amplitudes of up to 12 ms^{-1} throughout the mid- and high-latitudes.

Fig. 7d-f shows the latitude-time development of the SW1, SW2, and SW3 amplitudes from the FixedForcing experiment. The FixedForcing experiment employs a thermal forcing fixed to that of the 20th of December, while the background atmospheric variations are as in the full PRISM simulation. In addition, only the dominant SW2 forcing component is included, such that any non-migrating tides are the result of wave-wave interactions. The resulting SW1 tide closely resembles that of the OnlySolar simulation, reaching amplitudes of up to 24 ms^{-1} around day 45. The SW2 tide also displays similar characteristics to that of the OnlySolar simulation (Fig. 6d), with a 10-day amplitude minimum broadly centered on the day of peak PVW. The SW2 also shows a maximum around day 35, and a broad maximum after day 55. For the SW3 tide, the FixedForcing experiment identifies a pronounced non-linear wave-wave forcing occurring around day 45 between 50-60°N, reaching amplitudes of up to 18 ms^{-1}. However, since the thermal variations of the SW3 tide are similar in magnitude to those from the FixedForcing experiment, the wave-wave forcing response is difficult to uniquely separate from the full PRISM and OnlySolar simulations.

To isolate the impact of the changing propagation conditions through the zonal mean background atmosphere, the FixedForcingZM experiment repeats the FixedForcing experiment, but without the inclusion of planetary waves. Any variations in the SW2 amplitudes are then the result of variations in the zonal mean propagation conditions. Fig. 8 shows that the resulting SW2 follows that of the FixedForcing experiment, although amplitudes are generally higher at times when large non-migrating tides are present in the FixedForcing

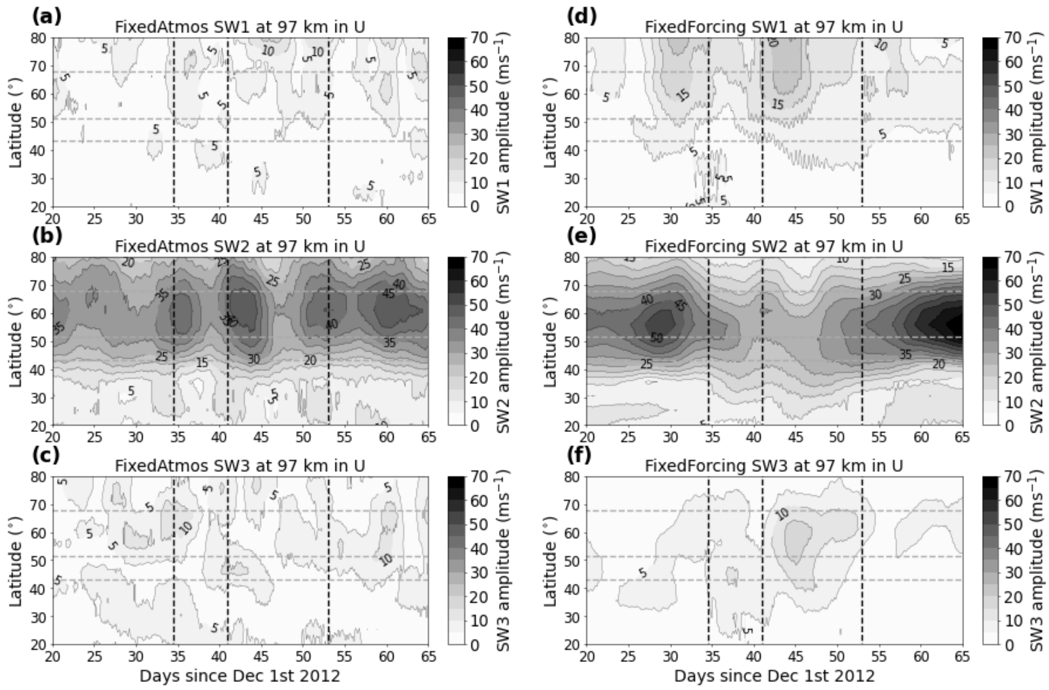

Figure 7. Latitude-time development of the zonal SW1, SW2, and SW3 amplitude at 97 km altitude for the FixedAtmos **(a,b,c)** and FixedForcing **(d,e,f)** experiments listed in Table 1. The vertical dashed lines mark the SSW onset, peak PVW, and recovery onset as defined in Section 2.1. The horizontal dashed lines mark the latitudes of the three meteor radars used in this study.

experiment (i.e., when the SW2 interacts with planetary waves). Nevertheless, the characteristic amplitude minimum centered roughly on the day of peak PVW is reproduced, along with the amplitude maxima around day 30 and after day 55.

4.2.1 Stratospheric Ozone

As discussed in Section 2, the employed IFS TTFs can not be used to describe the effects of a SSW-induced stratospheric ozone redistribution on the thermal SDT forcing. To determine the importance of this effect, a simulation is performed using 3-hourly TTFs from the SD-WACCMX model. The SD-WACCMX model includes parameterizations of all the major chemical and radiative processes from the surface to the thermosphere, and incorporates the instantaneous modeled stratospheric ozone distribution in its radiative transfer calculations. The model also captures the dynamics of the 2013 SSW, by virtue of its assimilated MERRA-2 reanalysis winds and temperatures for altitudes below ∼50 km.

To illustrate the effect of the SSW on the stratospheric ozone distribution, Fig. 9a shows the SD-WACCMX ozone mixing ratios at 40 km altitude on the day of peak PVW. Here a zonal wavenumber S = 1 structure is visible in the ozone mixing ratios between 40-50°N, which is shaped by the zonally asymmetric transport of ozone in response to the SSW. To isolate the impact of the ozone redistribution on the thermal SDT forcing, the WACStrat experiment includes only the SD-WACCMX TTFs between 100-0.1 hPa (10-70 km altitude), spanning the entire stratospheric ozone forcing region (van Caspel et al., 2022). Similar to the FixedAtmos experiment, the specified winds and temperatures of the background atmosphere are fixed to that of the 20th of December 2012 and include

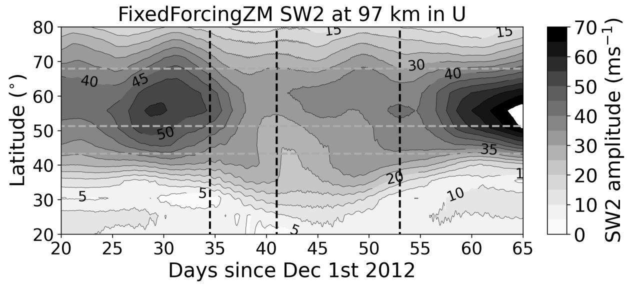

Figure 8. Latitude-time development of the zonal SW2 amplitude at 97 km altitude for the FixedForcingZM experiment listed in Table 1. The vertical dashed lines mark the SSW onset, peak PVW, and recovery onset as defined in Section 2.1. The horizontal dashed lines mark the latitudes of the three meteor radars used in this study.

no planetary waves. Any variations in the migrating and non-migrating tides can then be attributed to variations in the stratospheric ozone forcing itself.

Fig. 9b-d shows the time evolution of the SW1, SW2, and SW3 tidal amplitudes. The amplitude of the SW2 forcing response is decreased by 3-4 ms^{-1} about five days after peak PVW, while the SW1 component peaks at 2 ms^{-1} five days before peak PVW at 65°N. The largest variations occur in the SW3 component, which reaches amplitudes of up to 4-5 ms^{-1} five days before peak PVW at 50°N.

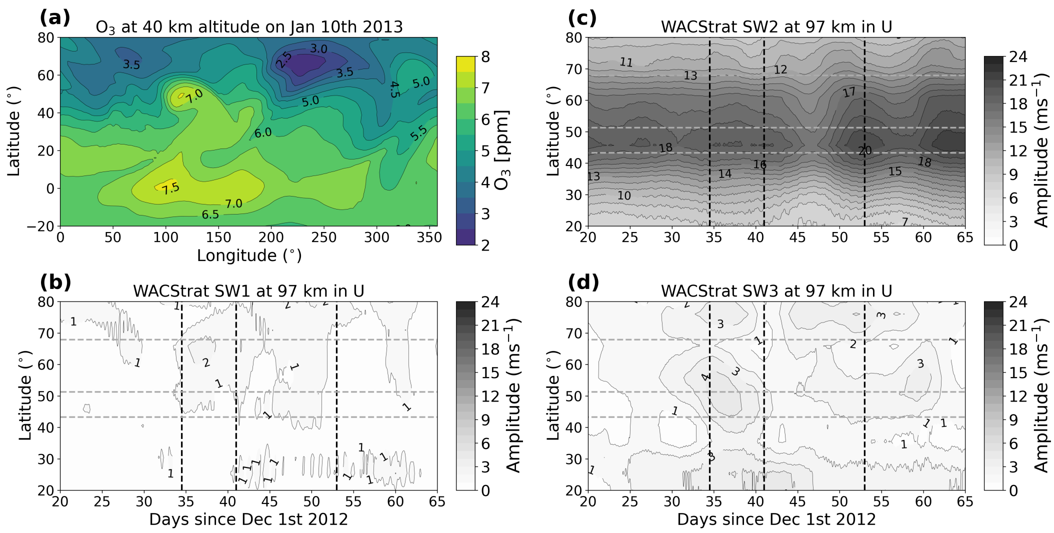

Figure 9. SD-WACCMX ozone mixing ratios at 40 km altitude on the 11th of January 2013 **(a)**, and the latitude-time development of the zonal SW1 **(b)**, SW2 **(c)**, and SW3 **(d)** amplitudes at 97 km altitude from the WACStrat experiment. Contours for the tidal amplitudes are spaced in 1 ms^{-1} intervals. The vertical dashed lines mark the SSW onset, peak PVW, and recovery onset as defined in Section 2.1. The horizontal dashed lines mark the latitudes of the three meteor radars used in this study.

5 Discussion and Conclusion

In this study, the SDT response to the 2013 SSW is simulated using the mechanistic PRISM tidal model. The model includes a detailed description of the lunar and solar tidal forcing terms, and the tides are propagated through a realistic background atmosphere based on the NAVGEM-HA meteorological analysis system. The simulated amplitude and phase variability of the SDT are found to be in close agreement with measurements made at the CMOR (43.3°N, 80.8°W), Collm (51.3°N, 13.0°E), and Kiruna (67.5°N, 20.1°E) radar sites between 80-97 km altitude. The SDT response is characterized by a 10-day amplitude minimum, followed by a 60-70 ms^{-1} amplitude maximum 5-10 days after peak PVW.

Numerical experiments where only the solar or lunar tidal forcing terms are included, find that the net simulated SDT response closely follows that of the solar component. During the time of the SDT enhancement, lunar amplitudes are around 10-15% of that of the solar component, reaching amplitudes of up to 12-14 ms^{-1} over the course of the SSW. Further numerical experiments find that the response of the solar SDT is governed by the changing zonal mean propagation conditions through the background atmosphere, and by non-linear wave-wave interactions between the SW2 tide and quasi-stationary planetary waves. The zonal mean propagation conditions shape the observed 10-day amplitude minimum, while non-migrating tides can contribute up to 50% of the net SDT amplitude during the enhancement following peak PVW. The impact of the SSW-induced redistribution of stratospheric ozone is found to be small, inducing amplitude variations of only up to 4 ms^{-1}.

In our results, the minimal role of the lunar SDT contrasts earlier reports of a strongly enhanced lunar SDT during the 2013 SSW, and during SSWs in general (e.g., Koushik et al., 2020; Conte et al., 2017; Chau et al., 2015; Xiong et al., 2013). We suggest that this discrepancy can be explained by the inherent difficulty of separating the solar and lunar SDT frequencies over the course of a SSW event. By way of illustration, the commonly used method of a 16-day sliding window fit containing both the 12.00 hr (solar) and 12.42 hr (lunar) SDT components is demonstrated, using the observed and simulated zonal winds at the CMOR radar site. The following results, however, also apply to window lengths anywhere between 14 to 21 days.

Fig. 10a,d shows the 16-day sliding window solar and lunar SDT amplitudes from the observed CMOR winds. The qualitative behavior of both tidal components follows that of the net observed SDT (Fig. 3a), showing strongly enhanced amplitudes around 5-10 days following peak PVW. Peak lunar amplitudes reach up to $\sim$24 ms^{-1}, and are nearly half that of the peak solar amplitudes. Applying the 16-sliding window fit to the CMOR winds simulated by PRISM shows similar results (Fig. 10b,e). The lunar amplitudes calculated for the PRISM simulation strongly contrast the results from Section 3.2, however, where the individual lunar tide simulation found amplitudes no greater than 14 ms^{-1}. That the high amplitudes calculated from the 16-day sliding window fit are instead caused by cross-contamination effects with the solar SDT, is illustrated in Fig. 10c,f. Here the 16-day sliding window analysis is applied to a simulation without a lunar tide forcing (OnlySolar). However, the same qualitative response for both the lunar and solar SDT components is reproduced, with lunar SDT amplitudes of up to 24 ms^{-1}. Similar analysis finds that the OnlySolar simulation yields cross-contaminated lunar SDT amplitudes of up to 24 ms^{-1} and 16 ms^{-1} at the Collm and Kiruna sites, respectively.

Diagnostic analysis where the 16-day sliding window fit is applied to the results from a simulation including only the thermal forcing and a fixed background atmosphere (FixedAtmos), find no evidence of lunar tide periodicities in the thermal forcing itself. It also finds no evidence of a (contaminated) lunar SDT response to the SSW. Applying the 16-day fit to a simulation with a fixed daily thermal forcing (FixedForcing) does, however, closely reproduce the cross-contaminated lunar tide enhancement. Thus indicating that the cross-contamination of the lunar SDT is caused by the SSW-induced variability in the propagation conditions of the solar SDT component. For example, the phase variation of the solar SDT over the 16 day window translates to a transient frequency variation. This in turn results in the bleeding of the 12.00 hr solar tide into the lunar spectral bandwidth.

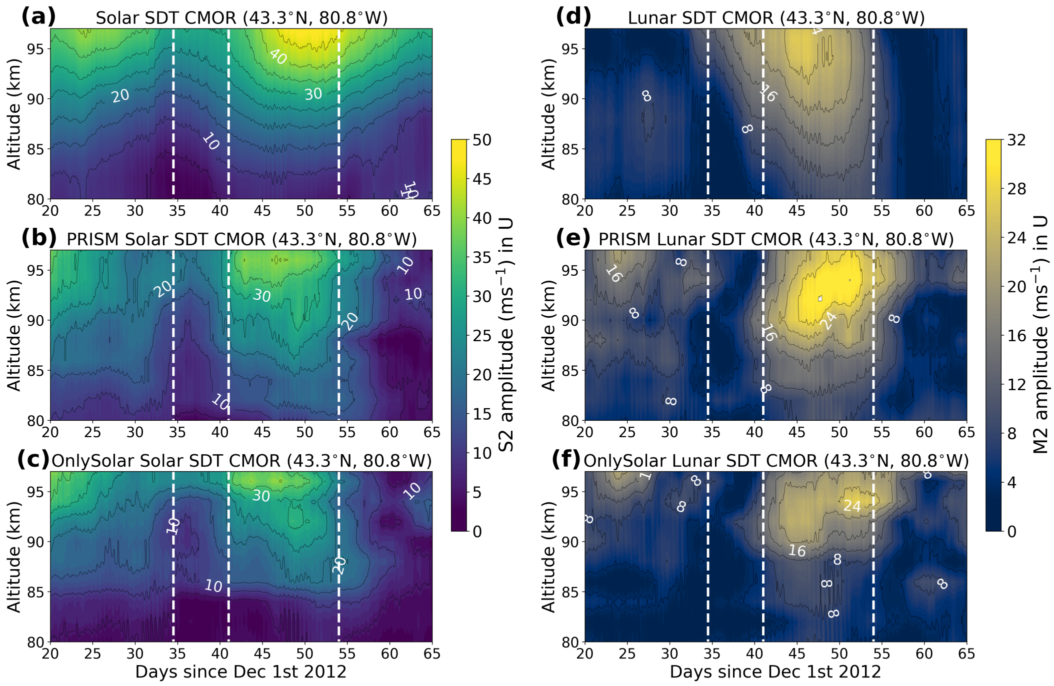

Figure 10. Solar and lunar SDT zonal amplitude calculated using a 16-day sliding window for the CMOR meteor winds **(a,d)**, PRISM simulation **(b,e)**, and OnlySolar experiment **(c,f)**. Note the different color scaling for the left-hand and right-hand panels. The vertical dashed lines mark the SSW onset, peak PVW, and recovery onset as defined in Section 2.1.

In summary, the SDT response to the 2013 SSW is found to be governed by that of the solar SDT component. This response is driven by the changing propagation conditions through the background atmosphere and by non-linear wave-wave interactions with quasi-stationary planetary waves. Non-migrating tides can contribute up to half of the net SDT response, suggesting that the SDT response at any given geographical location strongly depends on the planetary wave structure of the SSW. A climatological analysis of the SDT response at any location is therefore anticipated to require the sampling of a large number of events. In addition, the study of the SDT response is further complicated by the short-term variability of the solar component easily leading to an overestimation of the lunar amplitudes when both are separated over the course of a SSW. Future work will go out to studying the SDT response to other SSWs using the methodology outlined in this work, while also extending the analysis to other altitude regions.

Acknowledgments

The current research was supported by the Research Council of Norway (grant no. 223525/F50). The authors acknowledge the use of NAVGEM-HA data. Development of NAVGEM-HA was supported by the Chief of Naval Research and the Department of Defense High Performance Computing Modernization Project. CL acknowledges support by Deutsche Forschungsgemeinschaft (grant no. JA836/47-1).

Hourly ERA5 model level forecast data are available through the climate data store (CDS, `https://cds.climate.copernicus.eu`). SD-WACCMX data are available from `https://www.earthsystemgrid.org` CCSM run SD-WACCM-X v2.1, Atmosphere History Data, 3-Hourly Instantaneous Values, version 7.

The code used to compute FES2014 was developed in collaboration between Legos, Noveltis, CLS Space Oceanography Division and CNES, and is available under GNU General Public License.

The Esrange meteor radar operation, maintenance and data collection is provided by Esrange Space Center of Swedish Space Corporation.

This work was supported in part by the NASA Meteoroid Environment Office under cooperative agreement 80NSSC21M0073.

References

Angelats i Coll, M., & Forbes, J. M. (2002). Nonlinear interactions in the upper atmosphere: The s = 1 and s = 3 nonmigrating semidiurnal tides. *Journal of Geophysical Research: Space Physics*, *107*(A8), SIA 3-1-SIA 3-15. doi: https://doi.org/10.1029/2001JA900179

Arras, C., Jacobi, C., & Wickert, J. (2009). Semidiurnal tidal signature in sporadic e occurrence rates derived from gps radio occultation measurements at higher midlatitudes. *Annales Geophysicae*, *27*(6), 2555–2563. doi: 10.5194/angeo-27-2555-2009

Baldwin, M. P., Ayarzagüena, B., Birner, T., Butchart, N., Butler, A. H., Charlton-Perez, A. J., ... Pedatella, N. M. (2021). Sudden stratospheric warmings. *Reviews of Geophysics*, *59*(1), e2020RG000708. doi: 10.1029/2020RG000708

Chapman, S., & Lindzen, R. S. (1970). *Atmospheric tides.* Springer Netherlands. doi: https://doi.org/10.1007/978-94-010-3399-2

Charney, J. G., & Drazin, P. G. (1961). Propagation of planetary-scale disturbances from the lower into the upper atmosphere. *Journal of Geophysical Research (1896-1977)*, *66*(1), 83-109. doi: https://doi.org/10.1029/JZ066i001p00083

Chau, J. L., Hoffmann, P., Pedatella, N. M., Matthias, V., & Stober, G. (2015). Upper mesospheric lunar tides over middle and high latitudes during sudden stratospheric warming events. *Journal of Geophysical Research: Space Physics*, *120*(4), 3084-3096. doi: 10.1002/2015JA020998

Conte, J. F., Chau, J. L., Stober, G., Pedatella, N., Maute, A., Hoffmann, P., ... Murphy, D. J. (2017). Climatology of semidiurnal lunar and solar tides at middle and high latitudes: Interhemispheric comparison. *Journal of Geophysical Research: Space Physics*, *122*(7), 7750-7760. doi: https://doi.org/10.1002/2017JA024396

Coy, L., & Pawson, S. (2015, feb). The major stratospheric sudden warming of january 2013: Analyses and forecasts in the GEOS-5 data assimilation system. *Monthly Weather Review*, *143*(2), 491–510. doi: 10.1175/mwr-d-14-00023.1

Drob, D. P., Emmert, J. T., Meriwether, J. W., Makela, J. J., Doornbos, E., Conde, M., ... Klenzing, J. H. (2015). An update to the horizontal wind model (HWM): The quiet time thermosphere. *Earth and Space Science*, *2*(7), 301–319. doi: https://doi.org/10.1002/2014ea000089

ECMWF. (2020). Ifs documentation cy47r1 - part iv: Physical processes. In *Ifs documentation cy47r1.* doi: 10.21957/cpmkqvhja

Ehard, B., Malardel, S., Dörnbrack, A., Kaifler, B., Kaifler, N., & Wedi, N. (2018). Comparing ecmwf high-resolution analyses with lidar temperature measurements in the middle atmosphere. *Quarterly Journal of the Royal Meteorological Society*, *144*(712), 633–640. doi: 10.1002/qj.3206

Forbes, J. M. (2009). Vertical coupling by the semidiurnal tide in earth's atmosphere. *In T. Tsuda, R. Fujii, K. Shibata, & M. A. Geller (Eds.), Climate and Weather of the Sun-Earth System(CAWSES): Selected Papers from the 2007 Kyoto Symposium(pp.*

337–348). Tokyo: TERRAPUB.

Forbes, J. M., & Zhang, X. (2012). Lunar tide amplification during the january 2009 stratosphere warming event: Observations and theory. *Journal of Geophysical Research: Space Physics*, *117*(A12). doi: https://doi.org/10.1029/2012JA017963

Goncharenko, L., Chau, J. L., Condor, P., Coster, A., & Benkevitch, L. (2013). Ionospheric effects of sudden stratospheric warming during moderate-to-high solar activity: Case study of january 2013. *Geophysical Research Letters*, *40*(19), 4982-4986. doi: 10.1002/grl.50980

Goncharenko, L. P., Coster, A. J., Plumb, R. A., & Domeisen, D. I. V. (2012). The potential role of stratospheric ozone in the stratosphere-ionosphere coupling during stratospheric warmings. *Geophysical Research Letters*, *39*(8). doi: https://doi.org/10.1029/2012GL051261

Goncharenko, L. P., Harvey, V. L., Liu, H., & Pedatella, N. M. (2021). Sudden stratospheric warming impacts on the ionosphere–thermosphere system. In *Ionosphere dynamics and applications* (p. 369-400). American Geophysical Union (AGU). doi: https://doi.org/10.1002/9781119815617.ch16

Goncharenko, L. P., Harvey, V. L., Randall, C. E., Coster, A. J., Zhang, S.-R., Zalizovski, A., … Spraggs, M. (2022). Observations of pole-to-pole, stratosphere-to-ionosphere connection. *Frontiers in Astronomy and Space Sciences*, *8*. doi: 10.3389/fspas.2021.768629

Hagan, M. E. (1996, sep). Comparative effects of migrating solar sources on tidal signatures in the middle and upper atmosphere. *Journal of Geophysical Research: Atmospheres*, *101*(D16), 21213–21222. doi: https://doi.org/10.1029/96jd01374

Hersbach, H., Bell, B., Berrisford, P., Hirahara, S., Horányi, A., Muñoz-Sabater, J., … others (2020). The era5 global reanalysis. *Quarterly Journal of the Royal Meteorological Society*, *146*(730), 1999–2049. doi: https://doi.org/10.1002/qj.3803

Hibbins, R. E., Espy, P. J., Orsolini, Y. J., Limpasuvan, V., & Barnes, R. J. (2019). Superdarn observations of semidiurnal tidal variability in the mlt and the response to sudden stratospheric warming events. *Journal of Geophysical Research: Atmospheres*, *124*(9), 4862-4872. doi: https://doi.org/10.1029/2018JD030157

Hocking, W., Fuller, B., & Vandepeer, B. (2001). Real-time determination of meteor-related parameters utilizing modern digital technology. *Journal of Atmospheric and Solar-Terrestrial Physics*, *63*(2), 155-169. doi: https://doi.org/10.1016/S1364-6826(00)00138-3

Hollingsworth, A. (1971). The effect of ocean and earth tides on the semi-diurnal lunar air tide. *Journal of Atmospheric Sciences*, *28*(6), 1021 - 1044. doi: https://doi.org/10.1175/1520-0469(1971)028⟨1021:TEOOAE⟩2.0.CO;2

Jacobi, C., Fröhlich, K., Viehweg, C., Stober, G., & Kürschner, D. (2007). Midlatitude mesosphere/lower thermosphere meridional winds and temperatures measured with meteor radar. *Advances in Space Research*, *39*(8), 1278-1283. doi: 10.1016/j.asr.2007.01.003

Jin, H., Miyoshi, Y., Pancheva, D., Mukhtarov, P., Fujiwara, H., & Shinagawa, H. (2012). Response of migrating tides to the stratospheric sudden warming in 2009 and their effects on the ionosphere studied by a whole atmosphere-ionosphere model gaia with cosmic and timed/saber observations. *Journal of Geophysical Research: Space Physics*, *117*(A10). doi: https://doi.org/10.1029/2012JA017650

Koushik, N., Kumar, K. K., Vineeth, C., Ramkumar, G., & Subrahmanyam, K. V. (2020). Meteor radar observations of lunar semidiurnal oscillations in the mesosphere lower thermosphere over low and equatorial latitudes and their variability during sudden stratospheric warming events. *Journal of Geophysical Research: Space Physics*, *125*(9), e2019JA027736. doi: https://doi.org/10.1029/2019JA027736

Limpasuvan, V., Orsolini, Y. J., Chandran, A., Garcia, R. R., & Smith, A. K. (2016). On the composite response of the mlt to major sudden stratospheric warming events with elevated stratopause. *Journal of Geophysical Research: Atmospheres*, *121*(9), 4518-4537. doi: https://doi.org/10.1002/2015JD024401

Lin, J. T., Lin, C. H., Lin, C. Y., Pedatella, N. M., Rajesh, P. K., Matsuo, T., & Liu, J. Y. (2019). Revisiting the modulations of ionospheric solar and lunar migrating tides during the 2009 stratospheric sudden warming by using global ionosphere specification. *Space Weather*, *17*(5), 767-777. doi: https://doi.org/10.1029/2019SW002184

Liu, G., Lieberman, R. S., Harvey, V. L., Pedatella, N. M., Oberheide, J., Hibbins, R. E., … Janches, D. (2021). Tidal variations in the mesosphere and lower thermosphere before, during, and after the 2009 sudden stratospheric warming. *Journal of Geophysical Research: Space Physics*, *126*(3), e2020JA028827. doi: https://doi.org/10.1029/2020JA028827

Liu, H.-L., Bardeen, C. G., Foster, B. T., Lauritzen, P., Liu, J., Lu, G., … Wang, W. (2018). Development and validation of the whole atmosphere community climate model with thermosphere and ionosphere extension (WACCM-x 2.0). *Journal of Advances in Modeling Earth Systems*, *10*(2), 381–402. doi: https://doi.org/10.1002/2017ms001232

Liu, H.-L., Wang, W., Richmond, A. D., & Roble, R. G. (2010). Ionospheric variability due to planetary waves and tides for solar minimum conditions. *Journal of Geophysical Research: Space Physics*, *115*(A6). doi: https://doi.org/10.1029/2009JA015188

Liu, J., Zhang, D., Goncharenko, L. P., Zhang, S.-R., He, M., Hao, Y., & Xiao, Z. (2021). The latitudinal variation and hemispheric asymmetry of the ionospheric lunitidal signatures in the american sector during major sudden stratospheric warming events. *Journal of Geophysical Research: Space Physics*, *126*(5), e2020JA028859. doi: https://doi.org/10.1029/2020JA028859

Lyard, F. H., Allain, D. J., Cancet, M., Carrère, L., & Picot, N. (2021). Fes2014 global ocean tide atlas: design and performance. *Ocean Science*, *17*(3), 615–649. doi: 10.5194/os-17-615-2021

McCormack, J. P., Hoppel, K., Kuhl, D., de Wit, R., Stober, G., Espy, P., … Hibbins, R. (2017). Comparison of mesospheric winds from a high-altitude meteorological analysis system and meteor radar observations during the boreal winters of 2009–2010 and 2012–2013. *Journal of Atmospheric and Solar-Terrestrial Physics*, *154*, 132–166. doi: https://doi.org/10.1016/j.jastp.2016.12.007

Nath, D., Chen, W., Zelin, C., Pogoreltsev, A. I., & Wei, K. (2016). Dynamics of 2013 sudden stratospheric warming event and its impact on cold weather over eurasia: Role of planetary wave reflection. *Scientific Reports*, *6*(1). doi: 10.1038/srep24174

Pedatella, N. M., & Forbes, J. M. (2010). Evidence for stratosphere sudden warming-ionosphere coupling due to vertically propagating tides. *Geophysical Research Letters*, *37*(11). doi: https://doi.org/10.1029/2010GL043560

Pedatella, N. M., & Liu, H. (2013). The influence of atmospheric tide and planetary wave variability during sudden stratosphere warmings on the low latitude ionosphere. *Journal of Geophysical Research: Space Physics*, *118*(8), 5333-5347. doi: 10.1002/jgra.50492

Pedatella, N. M., Liu, H.-L., & Richmond, A. D. (2012). Atmospheric semidiurnal lunar tide climatology simulated by the whole atmosphere community climate model. *Journal of Geophysical Research: Space Physics*, *117*(A6). doi: https://doi.org/10.1029/2012JA017792

Pedatella, N. M., Liu, H.-L., Sassi, F., Lei, J., Chau, J., & Zhang, X. (2014). Ionosphere variability during the 2009 ssw: Influence of the lunar semidiurnal tide and mechanisms producing electron density variability. *Journal of Geophysical Research: Space Physics*, *119*(5), 3828-3843. doi: https://doi.org/10.1002/2014JA019849

Picone, J. M., Hedin, A. E., Drob, D. P., & Aikin, A. C. (2002). NRLMSISE-00 empirical model of the atmosphere: Statistical comparisons and scientific issues. *Journal of Geophysical Research: Space Physics*, *107*(A12), SIA 15–1–SIA 15–16. doi: https://doi.org/10.1029/2002ja009430

Stober, G., Baumgarten, K., McCormack, J. P., Brown, P., & Czarnecki, J. (2020). Comparative study between ground-based observations and navgem-ha analysis data in the mesosphere and lower thermosphere region. *Atmospheric Chemistry and Physics*, *20*(20), 11979–12010. doi: 10.5194/acp-20-11979-2020

Stober, G., Kuchar, A., Pokhotelov, D., Liu, H., Liu, H.-L., Schmidt, H., ... Mitchell, N. (2021). Interhemispheric differences of mesosphere–lower thermosphere winds and tides investigated from three whole-atmosphere models and meteor radar observations. *Atmospheric Chemistry and Physics*, *21*(18), 13855–13902. doi: 10.5194/acp-21-13855-2021

Stober, G., Liu, A., Kozlovsky, A., Qiao, Z., Kuchar, A., Jacobi, C., ... Mitchell, N. (2022). Meteor radar vertical wind observation biases and mathematical debiasing strategies including the 3dvar+div algorithm. *Atmospheric Measurement Techniques*, *15*(19), 5769–5792. doi: 10.5194/amt-15-5769-2022

Swinbank, R., & Ortland, D. A. (2003). Compilation of wind data for the upper atmosphere research satellite (uars) reference atmosphere project. *Journal of Geophysical Research: Atmospheres*, *108*(D19). doi: https://doi.org/10.1029/2002JD003135

Teitelbaum, H., & Vial, F. (1991). On tidal variability induced by nonlinear interaction with planetary waves. *Journal of Geophysical Research: Space Physics*, *96*(A8), 14169-14178. doi: https://doi.org/10.1029/91JA01019

van Caspel, W. E., Espy, P. J., Ortland, D. A., & Hibbins, R. E. (2022). The mid- to high-latitude migrating semidiurnal tide: Results from a mechanistic tide model and superdarn observations. *Journal of Geophysical Research: Atmospheres*, *127*(1), e2021JD036007. doi: https://doi.org/10.1029/2021JD036007

Vial, F., & Forbes, J. (1994, oct). Monthly simulations of the lunar semi-diurnal tide. *Journal of Atmospheric and Terrestrial Physics*, *56*(12), 1591–1607. doi: https://doi.org/10.1016/0021-9169(94)90089-2

Wu, Q., Ward, W., Kristoffersen, S., Maute, A., & Liu, J. (2019). Simulation and observation of lunar tide effect on high-latitude, mesospheric and lower thermospheric winds during the 2013 sudden stratospheric warming event. *Journal of Geophysical Research: Space Physics*, *124*(2), 1283-1291. doi: https://doi.org/10.1029/2018JA025476

Xiong, J., Wan, W., Ding, F., Liu, L., Ning, B., & Niu, X. (2013). Coupling between mesosphere and ionosphere over beijing through semidiurnal tides during the 2009 sudden stratospheric warming. *Journal of Geophysical Research: Space Physics*, *118*(5), 2511-2521. doi: https://doi.org/10.1002/jgra.50280

Zhang, J., Limpasuvan, V., Orsolini, Y. J., Espy, P. J., & Hibbins, R. E. (2021). Climatological westward-propagating semidiurnal tides and their composite response to sudden stratospheric warmings in superdarn and sd-waccm-x. *Journal of Geophysical Research: Atmospheres*, *126*(3), e2020JD032895. doi: https://doi.org/10.1029/2020JD032895

Zhang, X., & Forbes, J. M. (2014a). Lunar tide in the thermosphere and weakening of the northern polar vortex. *Geophysical Research Letters*, *41*(23), 8201-8207. doi: 10.1002/2014GL062103

Zhang, X., & Forbes, J. M. (2014b). Lunar tide in the thermosphere and weakening of the northern polar vortex. *Geophysical Research Letters*, *41*(23), 8201-8207. doi: https://doi.org/10.1002/2014GL062103